ADVANCED ELECTRONIC MATERIALS Open Access
www.advelectronicmat.de

Synaptic Function in Memristor Devices for Neuromorphic Circuit Applications

Juan Bisquert, Wooyoung Shim, So-Yeon Kim, and Bernabe Linares-Barranco*

The realization of artificial neural circuits requires synaptic materials and devices that show adaptation at different time scales to modulate signal transmission between neurons according to the desired applications. Sensory-motor and intelligence operation in the brain relies on the dynamical properties of synapses that adapt to the frequency and synchronization of voltage spikes. The properties of potentiation and depression of the synapse conductivity control the plasticity and adaptation of synapses. Here, the general dynamical properties of ionic or electronic current conduction that form the main rules of synaptic activity are discussed. The basic model requirements of a memristor or chemical inductor to produce an adaptation of conductance to incoming stimuli are established. The synaptic response can be described by the combination of three factors: A conduction process that depends on an internal state variable *x*; this variable causes rectification at an onset voltage; it also causes a memory, characterized by a delay in response to the stimulus. Diverse diagnosis methods are described that connect the nonlinear time response, the nonlinear cycling of current–voltage curves, and the linear frequency response of impedance spectroscopy, to assess the adaptation properties.

1. Introduction

Modern computers built on Von Neumann architecture are approaching their limits in terms of energy efficiency, especially when handling artificial intelligence algorithms and Internet of Things applications. Neuromorphic computing presents an alternative solution by mimicking the structure and function of the biological brain to enable more efficient learning and computation.[1–4] The fundamental building blocks for next-generation neuromorphic hardware are artificial neurons and synapses. Neurons serve as nodes that receive signals from other nodes, integrate inputs, and decide whether to pass the signal onward, as illustrated in **Figure 1a**. Synapses, which are specialized junctions where two neurons connect and communicate, control the filtering of signals, determining how information is processed and stored.

The contact strength of the synapse is flexible and can be modified according to the activities of the neurons that it connects. In the natural brain, a neuron generates an electrical signal called an action potential, which travels down its axon toward the synapse. When the signal arrives at the synapse, it releases neurotransmitters into the synaptic cleft (the gap between the neurons). The binding of neurotransmitters to receptors on the postsynaptic neuron triggers either excitatory or inhibitory responses, which determines the subsequent response. When a presynaptic neuron fires and successfully causes the postsynaptic neuron to fire (within a close time window), the synapse between them strengthens. This process is called long-term potentiation (LTP). If the presynaptic neuron frequently fires without causing the postsynaptic neuron to fire (i.e., there is little correlation between their activities), the synaptic connection weakens. This process is called long-term depression (LTD). These rules constitute the Hebbian synapse learning family, which is often stated as "cells that fire together, wire together."[5,6]

In artificial neuromorphic analog circuits, the signal between neurons is normally an electrical voltage and/or current that can have complex forms, as in spikes, consisting of repetitive pulses at a constant voltage amplitude. The artificial synapses have a property, as shown in Figure 1b, in which a memory state variable, termed x, modulates the conductance of the synapse, σ, which will provide the computational weights in a neural network

J. Bisquert, S.-Y. Kim
Instituto de Tecnología Química (Universitat Politècnica de València-Agencia Estatal Consejo Superior de Investigaciones Científicas)
Av. dels Tarongers, València 46022, Spain
E-mail: jbisquer@itq.upv.es

W. Shim
Department of Materials Science and Engineering
Yonsei University
Seoul 120-749, South Korea

W. Shim
Center for Nanomedicine
Institute for Basic Science (IBS)
Seoul 03722, South Korea

B. Linares-Barranco
Instituto de Microelectrónica de Sevilla
IMSE-CNM
(CSIC Universidad de Sevilla)
Sevilla 41092, Spain

The ORCID identification number(s) for the author(s) of this article can be found under https://doi.org/10.1002/aelm.202400903

DOI: 10.1002/aelm.202400903

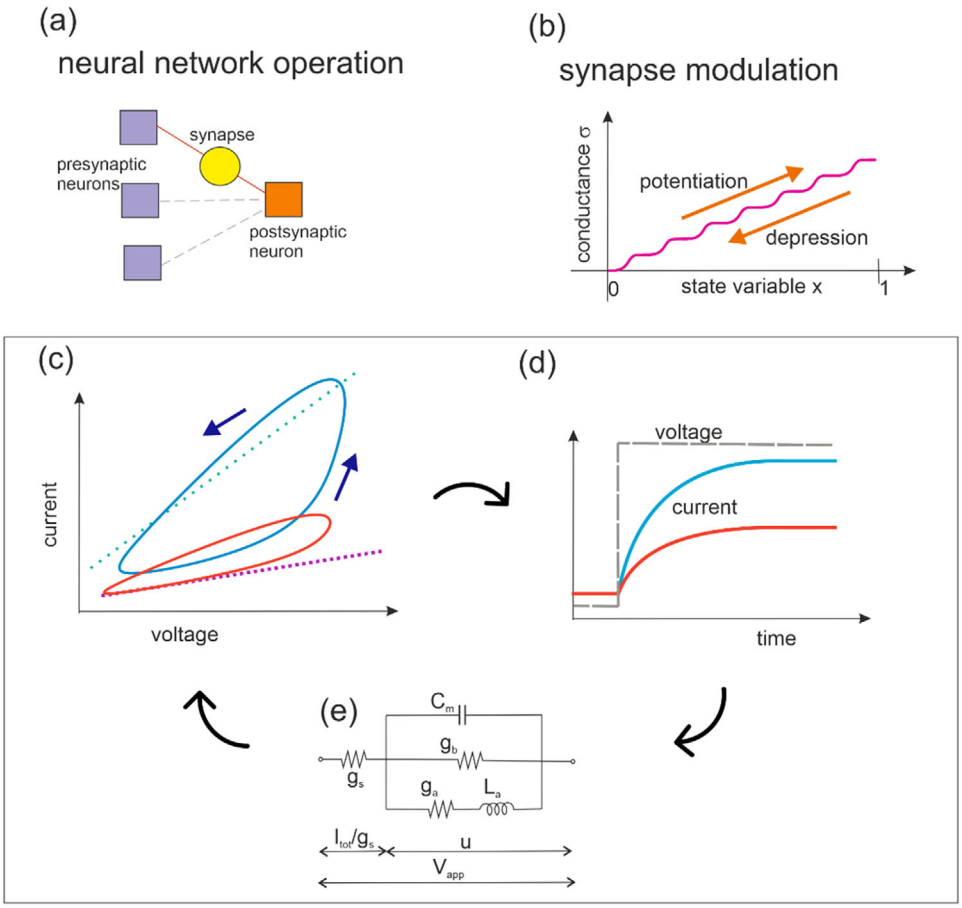

Figure 1. a) A schematic brain network system composed of neurons and synapses. The synapse weights the signal transmission from the presynaptic to the postsynaptic neurons. b) Conductance of synapses modulated by a state variable *x*, resulting in the synaptic properties of potentiation and depression. The squared panel diagrams show the relation of measurement techniques of a synaptic device: c) the current–voltage (*I*–*V*) curve. d) The time domain response to a voltage step and e) basic equivalent circuit under small ac perturbation.

link between neurons, as shown in Figure 1a. Furthermore, the synapse weight must be adapted by the incoming impulses, mimicking a Hebbian learning behavior. Therefore, the role of synapses is often taken by two-terminal memristor devices where the conductivity can be changed between two contacts by external stimuli.[5,7–12] Besides, three-terminal transistors are also widely used to form synapses, which can be operated by controlling the external stimulus through the third terminal, the gate electrode.[13–16]

Numerous resistive switching systems have been reported for analog volatile memory applications in neuromorphic systems.[17–22] They span a wide range of materials, including semiconductor ion carriers,[23–25] chalcogenide materials,[26] HfO_2,[27] metal oxides,[28,29] electrochemical metallization cells,[30] phase change materials,[31] halide perovskites,[32–36] fluidic nanochannels,[37–41] and biomaterials.[42] In typical two-contact memristors, the memory variable *x* is related to an ionic redistribution process that enhances the conductance, such as filamentary switching in electrochemical metallization (ECM) cells and valence change mechanism (VCM); interface-type switching by modification of Schottky barriers; and charge accumulation in fluidic nanochannels. The two-terminal synaptic memristors with controllable synaptic weights and spatiotemporal signal summation capabilities enable advanced computational functions,[5,27] as the vector-matrix multiplication in a crossbar array of memristors, logic gates,[41,43] and artificial neural networks with learning and recognition functions.[44]

We believe that the two-contact synapse devices across the varied material platforms share some basic dynamical characteristics that enable them to perform the synaptic function. It always involves a memory element, since the modified conductance must persist for a certain time, according to the retention time required in the computational system. Whatever the physical property that causes the memory in a variable of *x* type, such memory element must obey some basic rules to enable potentiation and depression.

In this paper, we provide a general view of the synaptic function approaching it from three different dynamical measurements, as outlined in Figure 1c–e: 1) the cycling of current–voltage (*I*–*V*) curves, in which the memory appears as hysteresis effects. 2) The small signal ac impedance, in which the delayed responses appear as capacitors and inductors. 3) The train of voltage pulses that form the potentiation and depression properties. We aim to establish a deep connection between these three

behaviors, which provides a powerful tool for characterizing new cases.

The aim of the paper is to illustrate the general dynamical properties that are common to most synaptic systems. In the next section, we find the characteristic behavior of artificial synaptic devices. Thereafter, in Section 3 we will describe some general properties of memristors that enable synaptic function.[45] Then, in Section 4 we provide a model that contains the main ingredients of the synaptic behaviors, based on a quasilinear property that will be suitably defined. This model describes well several types of memristors and clarifies the role of the different measurements, such as hysteresis curves (Figure 1c), that are discussed in Section 5, transient currents (Figure 1d), and their interpretation in terms of small signal equivalent circuit models (Figure 1d). In Section 6, we will discuss the main properties of cycling current–voltage,[45] the effect of relaxation times in volatility,[36] and how these memory effects enable interpretation of potentiation effects, based on the central role of the chemical inductor mechanism.[46] In Section 7, we discuss other situations involving more than one memory variable, that facilitate advanced biocomputational phenomena like activity-dependent thresholds. Finally, in Section 8, we extend the synaptic behavior to other type of stimuli, like optical signaling, that relies on a similar dynamic memory effect. We finish with a general discussion and conclusions.

2. Experimental Properties of Potentiation of Synaptic Devices

In this section, the main synaptic properties of potentiation and depression in different systems are summarized with specific examples. **Figure 2**a shows the properties of asymmetric fluidic nanochannels.[37,47] The ionic current through the channel is higher in forward than in reverse voltage. The rectification observed in quasiequilibrium $I-V$ curves is due to a difference in ion density in the wide and narrow extremes of the channel.[48] When the scan frequency is increased in Figure 2b, the current in the forward direction decreases, and the response displays hysteresis loops.[49]

In asymmetric nanochannels, the direction of ion transport is determined by the applied voltage polarity, leading to the simultaneous observation of rectification and hysteresis (Figure 2b). In Figure 2c,d, the change in pH causes a change of the sign of carriers in the channel wall. The combination of rectification and hysteresis produces a successive increase or decrease of the current under a train of voltage pulses. This is shown in Figure 2e, where the positive voltage stimulation produces potentiation, and the negative one produces depression. Then, the high current side occurs at negative potentials, and consequently, potentiation happens under negative voltage pulses (Figure 2f). These are the properties we wish to discuss in the next sections of the paper.

Figure 3 shows a similar experiment for a methylammonium lead bromide ($MAPbBr_3$) perovskite memristor.[50] The characteristic I–V response of the memristor device is shown in Figure 3a, while Figure 3b illustrates its dependence on vertex voltage. We can see in Figure 3c that the current raises inside one voltage pulse, but it depends on the applied voltage value (Figure 3d). This is because the system is stimulated at a high voltage (above a threshold voltage V_{th}), as observed in the hysteresis loops of Figure 3a, which show the self-crossing between 0.3 and 0.5 V, depending on the cycle velocity and the vertex voltage applied in the cycling.

In particular, Figure 3e,f shows that the potentiation transients have the same form as those for the fluidic channel in Figure 2. Figure 3g shows that the potentiation is gradual, which means that the state of the system is not forgotten from one pulse to the next, even though the measured current seems to decay to zero, both in the measurements of Figures 2 and 3. Note that we apply voltage zero between the pulses and we force the system to decay to a very small current. To track the evolution of the internal memory variable, a small *read* voltage is applied, as indicated in the inset of Figure 3f.[51,52] Then, we can obtain the remnant current after each pulse, which shows that potentiation occurs for steps of voltage $V > V_{th}$, while depression ensues when $V < V_{th}$, as indicated in Figure 3h. We remark that the discrete pulses are not necessary to observe potentiation; it can be obtained with a single long pulse as shown in Figure 3g.

The excitation/inhibition of the synaptic device can be obtained with different types of devices in **Figures 4** and **5**. Figure 4a exhibits the nonlinear synaptic transmission characteristics of the two-terminal, bilayer InGaZnO (α-IGZO)-based memristor. Potentiation and depression characteristics are shown in Figure 4a, in which successive applied electric fields make the device reach increasing (decreasing) conductance during the positive (negative) voltage sweeps. Also, the successive triangular voltage ramps increase/decrease the conductivity depending on the time, and the change of the synaptic conductivity according to the sweep cycles is shown.

The velocity of potentiation also depends on the polarization time Δt_p (the pulse width) and resting time Δt_r (the inter-pulse time). The release of neurotransmitters in the synaptic junction is caused by the arrival of action potentials generated by firing, and then a signal is transmitted as a synaptic potential. Frequent stimulation causes long-term enhancement in the strength of the synaptic connection. This tendency results in frequency dependence properties of the stimulation for a WO_{3-x}-based ionic device (Figure 4b),[29] an Ag_2S inorganic synapse (Figure 5a),[53] and a single crystal perovskite memristor (Figure 5b).[34] Note in Figure 5a that the stimulus is applied for a short pulse, and then the strength of potentiation depends on the rest time. For a long rest time ($\Delta t_r = 20$ s), the conductance is only transiently increased without reaching a stable potentiation, while for the reduced rest time ($\Delta t_r = 2$ s), a stable potentiation is obtained. Similar results can be observed in Figure 4b.

These frequency-dependent properties provide the mimicking of biology-like synaptic properties,[5,6] as the short-term and long-term plasticity, the spike-rate-dependent plasticity (SRDP), and the paired-pulse facilitation (PPF)[54] shown in Figure 5b. The spike-timing dependent plasticity (STDP)[11,23,25,55–60] rely on the ordered match of action potentials in pre and postsynaptic neurons. To reproduce STDP, a pair of pulses with positive and negative amplitude can be applied to each electrode, simulating the correlation of spikes,[25] and realistic forms of the action potential can be implemented.[56,60–63] This is illustrated in **Figure 6**. Other functions can be measured as the paired-pulse depression (PPD), the spike voltage-dependent plasticity (SVDP), spike number-dependent plasticity (SNDP), and spike frequency-dependent plasticity (SFDP).

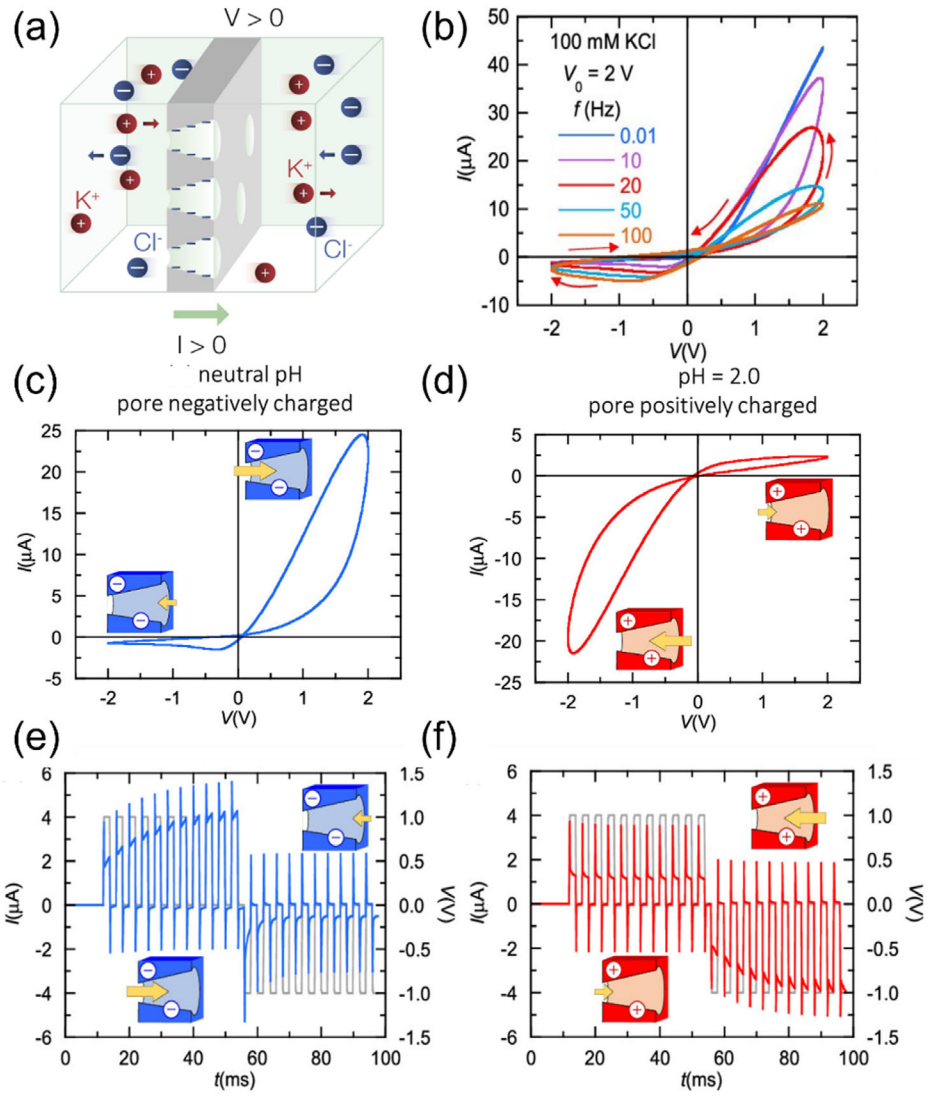

Figure 2. a) Ion conduction through multipore polyethylene terephthalate (PET) membranes. b) *I–V* curves in 100 mM KCl solution at neutral pH, parametrically in the electrical potential scan rate, characterized by the signal frequency $f_\Omega = \Omega_s / 2\pi$ with a voltage amplitude of 2 V. The arrows indicate the signal time evolution. *I–V* curves for c) neutral pH and d) pH = 2.0. e) Current response (left) to a sequence of 2 ms positive voltage pulses (right) showing a gradual conductance potentiation followed by a sequence of negative voltage pulses, which reset the multipore membrane to the low conductance state for neutral pH. f) Same experiment except for pH = 2.0. In all cases, V_0 = 1 V and c = 50 mM KCl. Reproduced with permission.[33] Copyright 2023, American Chemical Society.

Depending on the specific synapse device dynamic equations, it is possible to engineer different spike shapes to induce specific STDP learning rules, as illustrated in **Figure 7**. In the Bienenstock–Cooper–Munro (BCM) learning rule[64,65] that describes many aspects of experience-dependent plasticity in the developing visual cortex, a crossover point occurs between LTD-LTP that varies as a function of the history of cortical activity.[66]

3. Main Synaptic Processes

3.1. Memory-Controlled Conductance: Memristors

The essential property of the synapse is a signal transmission system with memory in which positive/negative pulses are used to excite/inhibit the synapse's weight property. There are different types of transmission properties, e.g., optical transmittance, and several possibilities are discussed in Section 8. However, in the first sections of the paper, we will adopt the most extended property, which is electrical conductivity in an electrical array. Therefore, a modulation of the conductance is a dominant feature, and we are led to systems that show resistive change.[12,67–70]

We will use a model of the type[7,8,46]

$$I_{tot} = f(V, x) \tag{1}$$

$$\tau_k(V)\frac{dx}{dt} = g(V, x) \tag{2}$$

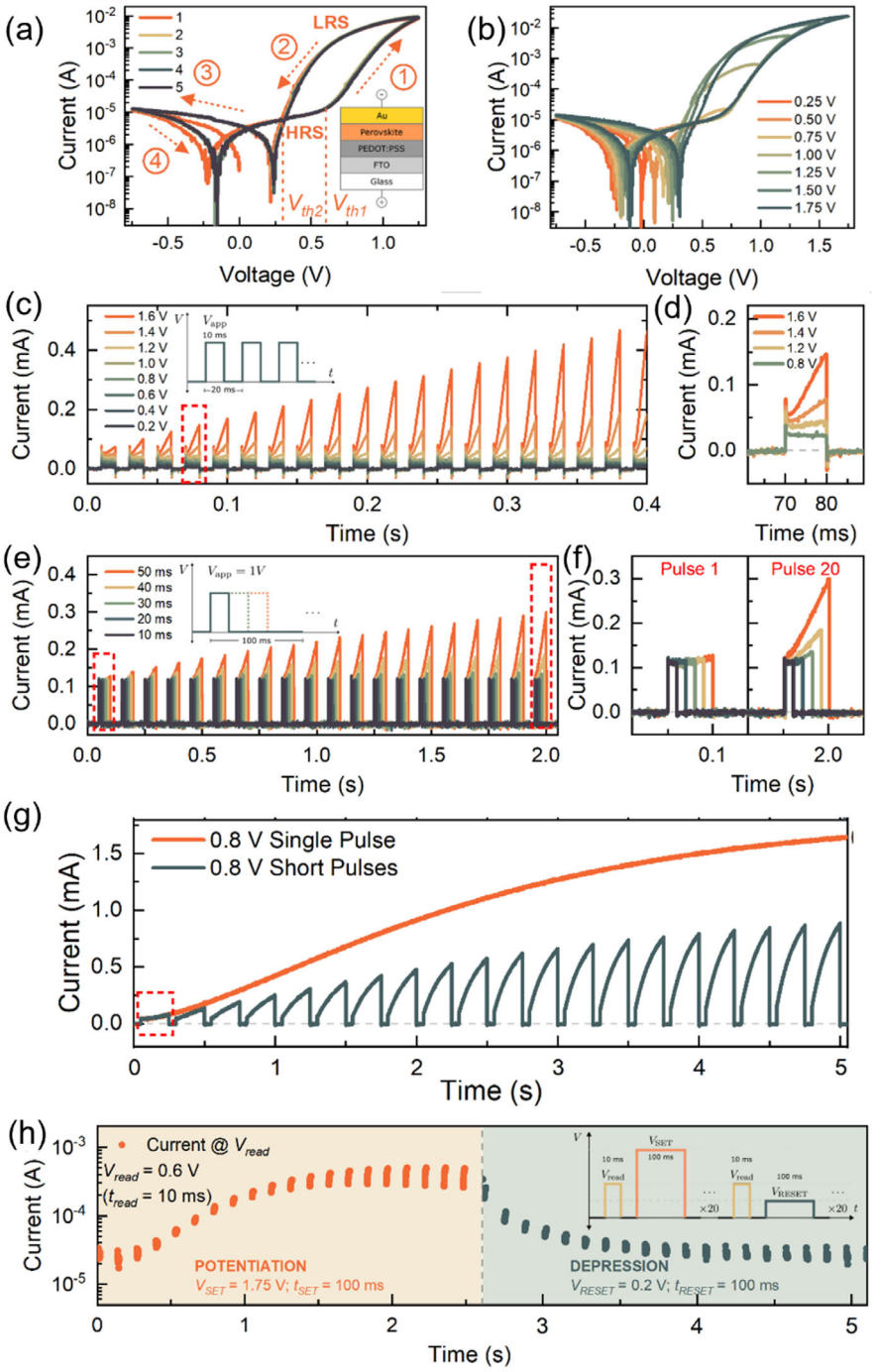

Figure 3. a) The characteristic *I–V* response of the memristor device over 5 cycles at a scan rate of 1 V s^{-1}, shown on a semilog scale, exhibiting a threshold resistive switching. Arrows and numbers indicate the scan direction. The inset illustrates a schematic diagram of the device configuration (FTO/PEDOT:PSS/$MAPbBr_3$/Au). b) Voltage-dependent multilevel/multistate analog resistive switching of the memristor device. c) The voltage-dependent transient current response of methylammonium lead bromide perovskite memristor by applying 20 identical voltage pulses with an amplitude of V_{app} and a pulse width of 10 ms (schematic diagram shown in inset) and d) the magnified view of the transient current response of a single voltage pulse at representative V_{app} levels. e) The pulse width-dependent transient current response by applying 20 identical voltages pulses with a period T_{pulse} of 100 ms and f) the corresponding magnified view of the first and last transient responses. g) Comparison of the transient current response of the volatile perovskite memristor with a single long pulse (5 s) and a train of 20 identical short pulses (pulse width of 200 ms; pulse period of 250 ms) at applied voltage 0.8 V, and h) the synaptic potentiation and depression characteristic response of the memristor measured at a read voltage V_{read} = 0.6 V (pulse width t_{read} = 10 ms), SET voltage V_{SET} = 1.75 V (pulse width = 100 ms), and a RESET voltage V_{RESET} = 0.2 V (pulse width = 100 ms) with the inset illustrating the schematic diagram of the pulsed measurement sequence. Reprinted with permission from under the terms of the Creative Commons Attribution (CC BY 4.0) license.[50]

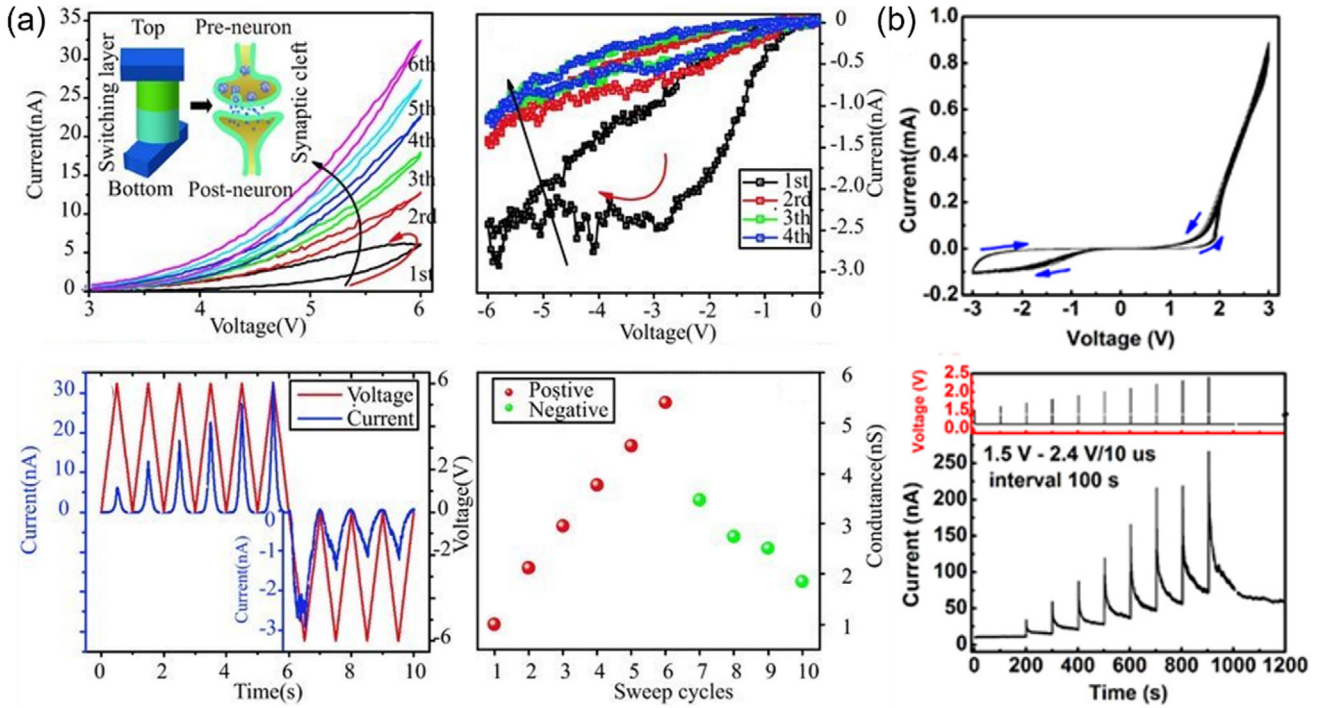

Figure 4. a) The nonlinear transmission characteristics of InGaZnO (α-IGZO) memristor. *I–V* characteristics of the memristor at positive and negative bias voltages for potentiation and depression, the voltage sweep range is from zero to + 6 V then back (−6 V) to zero with the time of 1 s for a sweep cycle (above two figures). The ramps of current and voltage versus time and the variation of the device conductivity with the scanning sweep cycles (bottom two figures). Reproduced with permission.[25] Copyright 2012, John Wiley and Sons. b) Nonvolatile resistive switching behavior and memorization in a WO_{3-x}-based nanoionics device. Above typical *I–V* characteristics of nonvolatile resistance switching behavior observed on the device after the forming process and nonvolatile memorization obtained by applying a sequence of electric pulses with increasing amplitude from 1.5 to 2.4 V with a step of 0.1 V for 10 µs and a pulse interval of 100 s. Reproduced with permission.[29] Copyright 2013, IOP Publishing.

Here I_{tot} is the total current. f is a conductivity function that describes the conduction current, with respect to voltage V in the device and a state variable x. The x is a (memory) variable necessary to determine the future behavior of the system when the present state and the inputs are known. For simplicity, we consider that x is a normalized variable $0 \leq x \leq 1$. The delay effect is expressed in Equation (2), indicating that changes of the "slow" state variable x are controlled by an adaptation function $g(V, x)$ with the characteristic time τ_k. More generally, the device can be controlled by several state variables x_i,[8] and these systems will be addressed in Section 7.

The stationary conduction under constant voltage V_{dc} will be established when $dx/dt = 0$. Then

$$I_{dc} = f\left(V_{dc}, x_{eq}\right) \tag{3}$$

where $x_{eq}(V)$ is the equilibrium value of the memory variable at the applied voltage that is obtained by the solution of

$$g\left(V_{dc}, x_{eq}\right) = 0 \tag{4}$$

Typically, x_{eq} has a sigmoidal form, and the x will control the system conductance, as indicated in Figure 1b, say from a low conductance at $x = 0$ with current $I_{cond}(V,0)$, to a high conductance at $x = 1$ with much higher current, $I_{cond}(V,1) \gg I_{cond}(V,0)$. This transformation is the *set* process in the resistive switching, which forms a potentiation effect, and the reverse process ($x = 1 \rightarrow 0$) is the *reset* that brings the system back to a low conductance state, causing conductance depression.

We remark that in synapse applications, it is desirable that the system persists at intermediate values of x, between 0 and 1. The change of synaptic weight σ can be viewed as a change in current under the *read* voltage as follows[71]

$$\Delta\sigma = \left|\frac{I_1 - I_0}{I_0}\right| \tag{5}$$

Here I_0 is the initial current and I_1 after the application of a stimulus that changes the weight. In the *read* current I_1, one uses a low amplitude voltage so as not to alter the state/conductance of the memristor. In general, we have a correlation $\sigma(x)$ for using the memristor as a synapse.

3.2. The Process of Potentiation: Chemical Inductors

Each potentiation step is determined by two factors:

1) a voltage step shifts the equilibrium function value $x_{eq}(V_0) \rightarrow x_{eq}(V_1)$, and
2) the new conductance-determining state, $x_{eq}(V_1)$, is established during the relaxation time, $\tau_k(V_0, V_1)$.

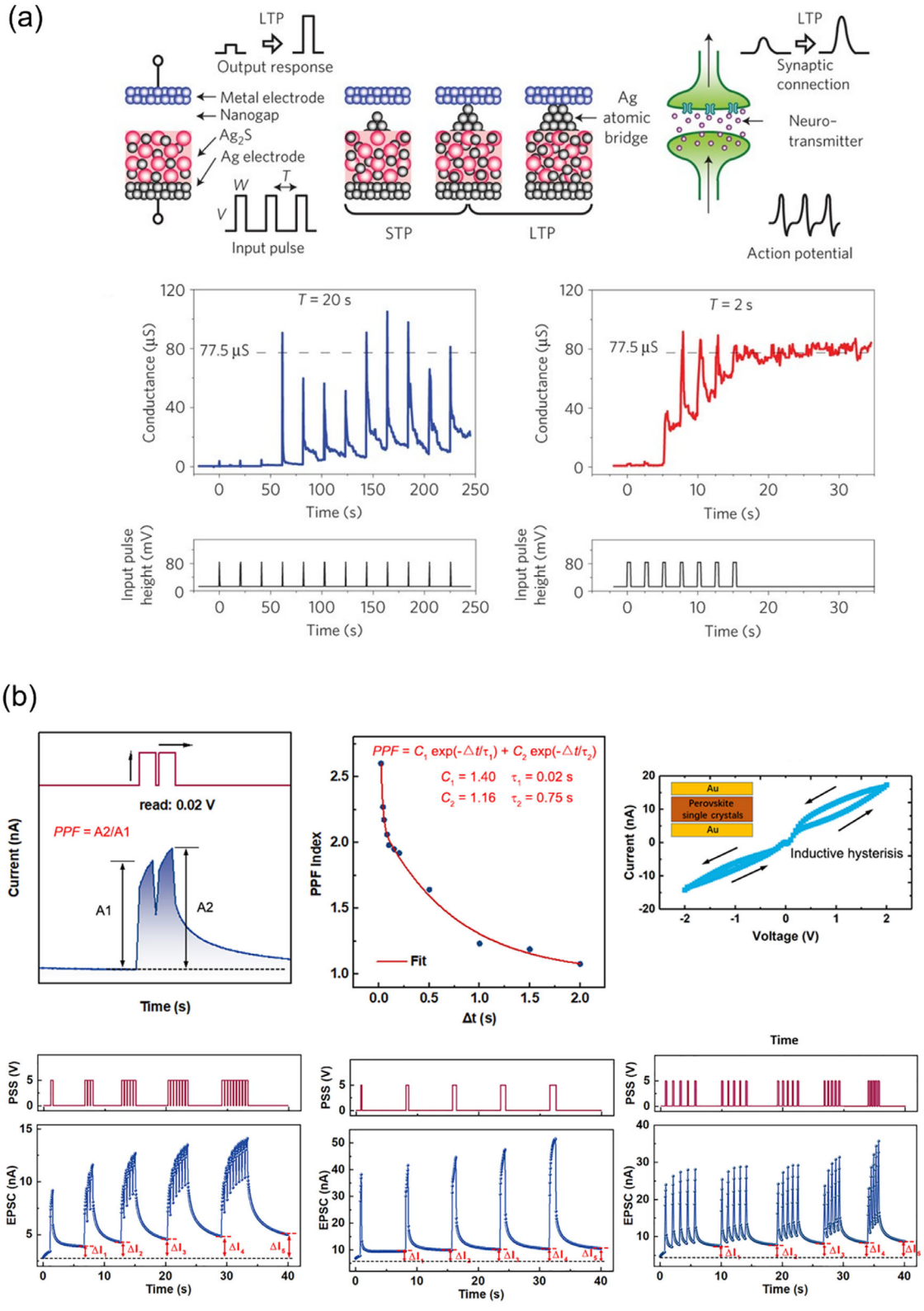

Figure 5. a) Conductance changes along with applied input pulses ($V = 80$ mV, $W = 0.5$ s) at the intervals of $T = 20$ s and 2 s in Ag_2S-based inorganic synaptic system. The conductance of the inorganic synapse with a single atomic contact is $2e^2/h$ (= 77.5 μS), where e is the elementary charge, and h is Planck's constant. Reproduced with permission.[53] Copyright 2011, Springer Nature. b) Synaptic behavior of a single crystal (SC) halide perovskite memristor composed of Au/$MAPbBr_3$ SC/Au, in which paired-pulse facilitation (PPF), inductive I–V hysteresis characteristic, and number-duration-frequency dependence of the pre-synaptic spikes are described. Reproduced with permission.[34] Copyright 2024, Elsevier.

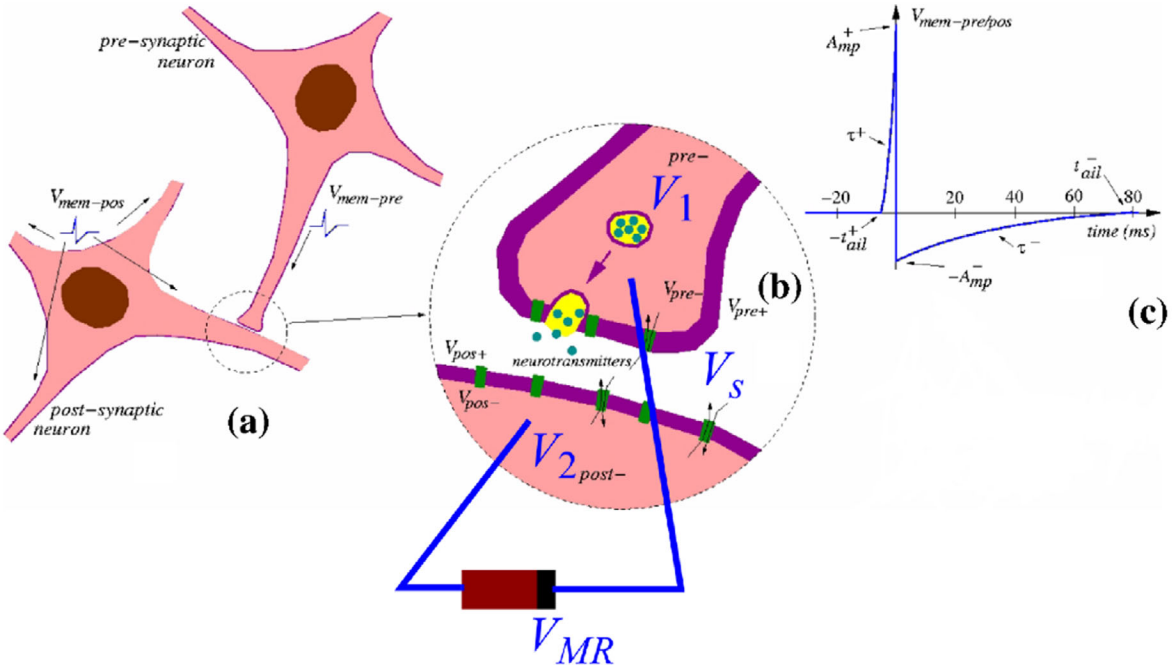

$$V_{mem\_pre} = V_s - V_1$$
$$V_{mem\_pos} = V_s - V_2$$
$$V_{MR} = V_1 - V_2 = V_{mem\_pos} - V_{mem\_pre}$$

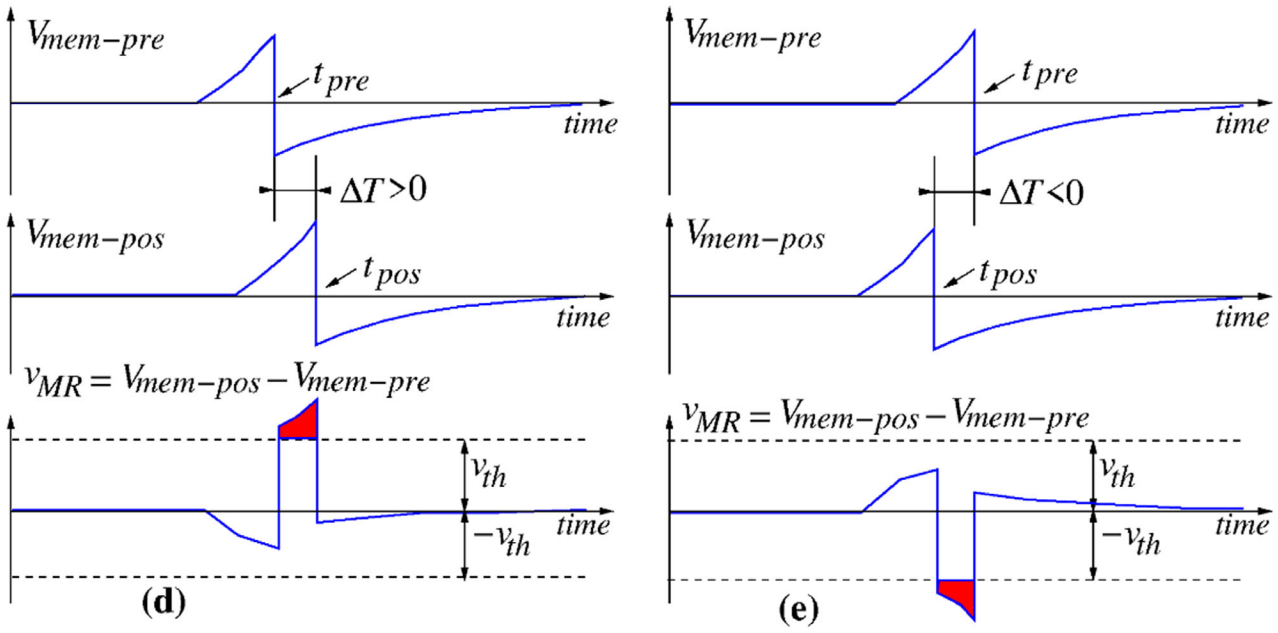

Figure 6. Illustration of STDP learning with memristors with special spike shapes. a) Pre- and postsynaptic neurons connected through a synapse. b) Detail of synapse. Inside of presynaptic cell is at voltage $V_{pre-} = V_1$, outside is at $V_{pre+} = V_s$, inside of postsynaptic cell is at $V_{pos-} = V_2$, outside is at $V_{pos+} = V_s$. A memristor can be thought as being connected between V_2 and V_1. Presynaptic neuron voltage is $V_{mem\_pre} = V_s - V_1$, postsynaptic neuron voltage is $V_{mem\_pos} = V_s - V_2$. Memristor voltage is $V_{MR} = V_{mem\_pos} - V_{mem\_pre}$. c) Pre- and postsynaptic neuron transmit spikes with positive peak and negative tail. d) If postsynaptic spike happens after presynaptic spike ($\Delta T > 0$), V_{MR} can have a high positive value, inducing LTP. e) If presynaptic spike happens after postsynaptic spike ($\Delta T < 0$), V_{MR} can have a high negative value, inducing LTD. Reproduced with permission from[60] licensed under a Creative Commons Attribution (CC BY 4.0) license.

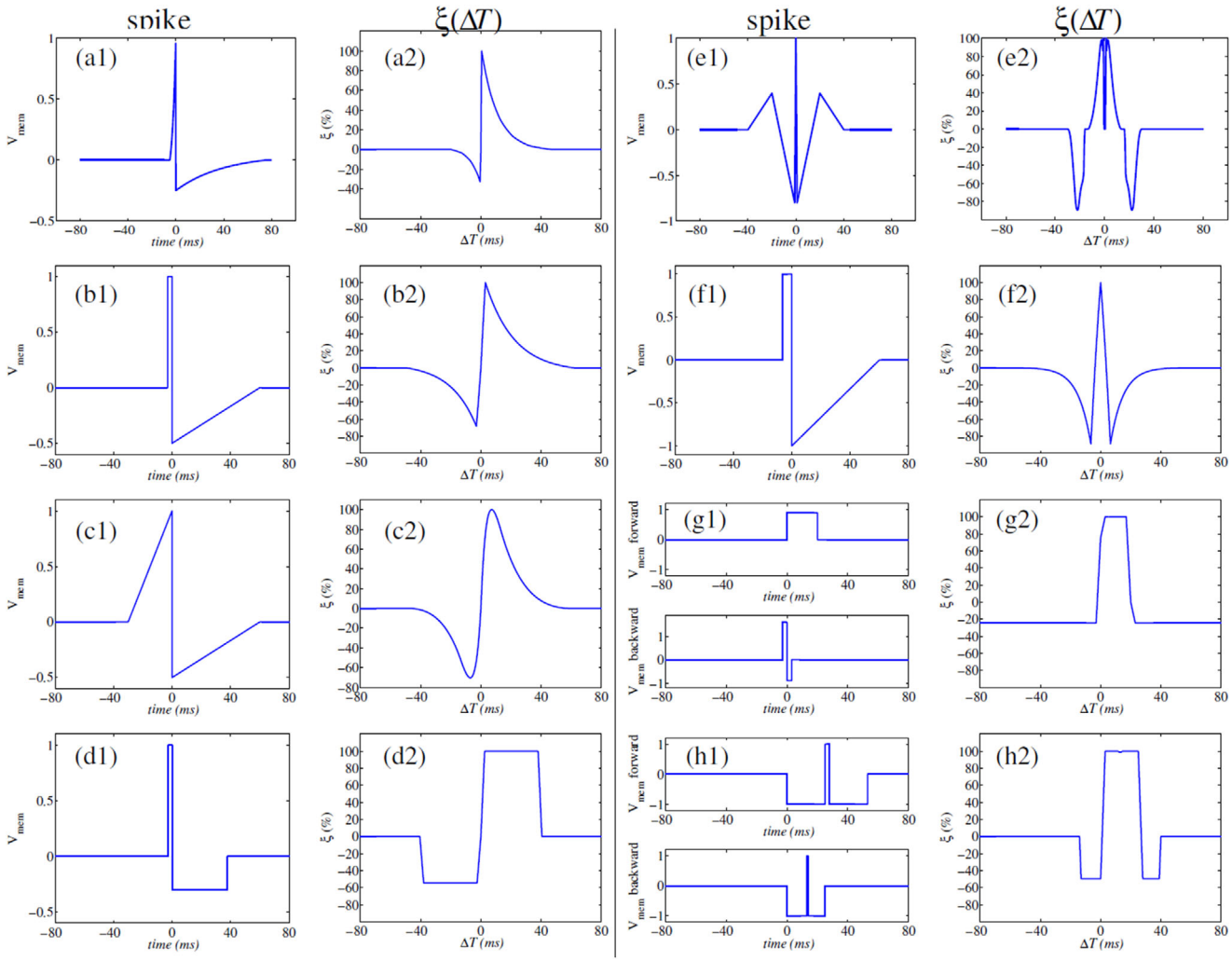

Figure 7. Engineering of spike waveforms to obtain different STDP learning functions to update the synaptic weight w, $\Delta w = \xi(\Delta T)$, with ΔT being the time difference between the post- and presynaptic spikes. Reproduced with permission from[11] licensed under a Creative Commons Attribution (CC BY 4.0) license.

This combination causes an increase in *current* over time, indicating that the core mechanism of the synapse is an *inductive* process.[45] This inductive process, described by the Equations (1) and (2), is associated with the transition between two intrinsic conduction possibilities of the system: from the lower, "fast" branch to the higher, "full" conduction current. We have generally termed such systems chemical inductor,[46] as they appear in different branches of science, e.g., catalysis and batteries. The dynamics of the chemical inductor in halide perovskite memristors have been explained in recent publications.[72–76]

3.3. A Generative Example: Hodgkin–Huxley Model

The models satisfying the types of Equations (1) and (2) apply in a broad variety of systems, for example in metal-oxide synaptic devices,[77–79] and various biological systems, such as the Hodgkin–Huxley (HH) model for the action potential in the neuron axon,[80–83] and other biological channels and pores that are crucial in numerous physiological processes.[84–86]

While HH model is an example of a spiking neuron system, the model structure is very useful for conductance-controlled synapses elements that are the main focus of this work. The HH model is based on the following equations

$$I_{\text{tot}} = C_{\text{m}}\frac{du}{dt} + g_{\text{Na}}m^3h\left(u - E_{\text{Na}}\right) + g_{\text{K}}n^4\left(u - E_{\text{K}}\right) + g_{\text{leak}}\left(u - E_{\text{leak}}\right) \quad (6)$$

$$\tau_{\text{m}}(u)\ \frac{dm}{dt} = m_{\text{eq}}(u) - m \quad (7)$$

$$\tau_{\text{h}}(u)\ \frac{dh}{dt} = h_{\text{eq}}(u) - h \quad (8)$$

$$\tau_{\text{n}}(u)\ \frac{dn}{dt} = n_{\text{eq}}(u) - n \quad (9)$$

Equation (6) relates the current I_{tot} and the voltage u across the neuron wall, $u = V - V_{\text{R}}$, where $V_{\text{R}} = -65$ mV is the rest

voltage of the membrane. It contains a capacitive charging with the capacitance C_m of the neuron wall. The next three terms correspond to generalized Ohm's law for three conduction channels: the sodium-selective channel, the potassium-selective channel, and a leak channel, with conductances g_{Na}, g_K, g_{leak} and the equilibrium potentials E_{Na}, E_K, E_{leak}. The current across the channel is also controlled by gating variables m, h, n. m, h determine activation and deactivation of the sodium channel, and n activates the potassium channel. We remark that HH contains in Equations (7–9) three chemical inductor variables of the type (2), with the respective equilibrium functions and relaxation times τ_k, that will be further discussed in Section 4.

Due to the similarity of mechanisms of HH neurons and memristors, one can obtain a variety of spiking systems starting from Equations (1) and (2). However, spiking requires special dynamical stability properties that are usually caused by negative resistance effects,[87,88] which are not needed in synaptic devices.

4. The Conductance-Activated Quasilinear Memristor (CALM) Model

To analyze the different properties that we have outlined in Figure 1, we use a relatively simple model of the type (Equations (1) and (2)) in which the memory variable is a normalized conductance x that switches the system between low and high conductance states.[49,89] Therefore, we have $x = \sigma$ in Equation (5), and the synaptic weight is directly recorded by the state variable. The model has application in experimental systems, *e.g.*, the fluidic nanochannels of Figure 2,[49,89,90] the halide perovskite memristors of Figure 3,[91] and solid-state memristors.[92]

4.1. Features of the Model

The first part of the model is formed by the equations

$$V_{app} = I_{tot}\ /g_s + u \tag{10}$$

$$I_{tot}\ (u) = \left[g_L + \left(g_H - g_L\right) x\right]\ u + C_m \frac{du}{dt} \tag{11}$$

Equation (10) separates the applied voltage V_{app} into the voltage in a series conductance g_s induced voltage, and the voltage u in the active part of the device. The total current in Equation (11) includes the conduction current (where g_L and g_H represent the conductance values at low and high states, respectively) and the capacitive current associated with the geometric or contact capacitance $C_m > 0$, present in most devices. Accordingly, there is a "fast" initial relaxation for the transient time of the charging, $\tau_m = R_s\ C_m$, where R_s is a resistance in the system such as a series resistance $R_s = 1/g_s$. As discussed previously, the conduction current

$$I_{cond}\ (u) = \left[g_L + \left(g_H - g_L\right) x\right]\ u \tag{12}$$

makes a change from a low value g_L to a high value g_H. This happens when the activation function passes from $x = 0$ to $x = 1$, as shown in **Figure** 8a. The adaptation equation has the form

$$\tau_k\,(u)\ \frac{dx}{dt} = x_{eq}\ (u) - x \tag{13}$$

so that in equilibrium $x \to x_{eq}$. As mentioned before, Equations (12) and (13) are the essential form of a chemical inductor[46] and also the typical constitutive equations of memristors.[7,8]

The model approach (12–13) has some special properties. It is linear on the conductance x-variable, though not in u-variable (the nonlinearity happens in the functions $x_{eq}(u)$ and $\tau_k\,(u)$). Due to this feature, integration of some dynamical properties is simplified, as further discussed in Sections 5 and 6. Nevertheless, this type of model can produce highly sophisticated dynamic behaviors, and it is widely used in neuronal dynamics.[93] To indicate these restriction properties we denote the model a conductance-activated quasilinear memristor (CALM) model. An analysis of the limitations of these assumptions is provided in Section 7.

Specific material properties of a CALM model are determined by two functions. The first is the equilibrium function x_{eq}. Here, we choose a sigmoidal form

$$x_{eq} = \frac{1}{1 + e^{-\left(u - V_{Bx}\right)/V_m}} \tag{14}$$

as shown in Figure 8c. V_{Bx} is a threshold potential for the activation of x, and the voltage V_m describes the steepness of the transition. This form is quite typical in many solid-state fluidical and biological systems.[92]

The final piece of the model is the voltage dependence of the relaxation time, $\tau_k(u)$, which has a profound impact in the dynamical properties of switching devices and synapses.[94] Here, we adopt the form

$$\frac{1}{\tau_k} = \frac{1}{\tau_M} + \frac{1}{\tau_0}\left(e^{\frac{u - V_A}{n_A V_m}} + e^{-\frac{u - V_D}{n_D V_m}}\right) \tag{15}$$

The relaxation time contains two exponential winds for activation and deactivation, as shown in **Figure** 9a,b.[49] It has a kinetic constant τ_0, onset parameter V_A, and ideality factor n_A, and deactivation voltage V_D with ideality factor n_D. The parameters n_A, n_D make the activation and deactivation wings of the relaxation time more or less steep. These parameters satisfy the constraint

$$\frac{1}{n_A} + \frac{1}{n_D} = 1 \tag{16}$$

The peak of the relaxation time is at the voltage

$$V_{Br} = \frac{V_A}{n_A} + \frac{V_D}{n_D} \tag{17}$$

The form in Figure 9a is flattened to the limiting value τ_M.

4.2. Interpretation of the Relaxation Time

The main reference for the features of the relaxation time originates from HH model for the protein channels in neurons, outlined in Equations (7–9).[80–83] The relaxation times of the gating

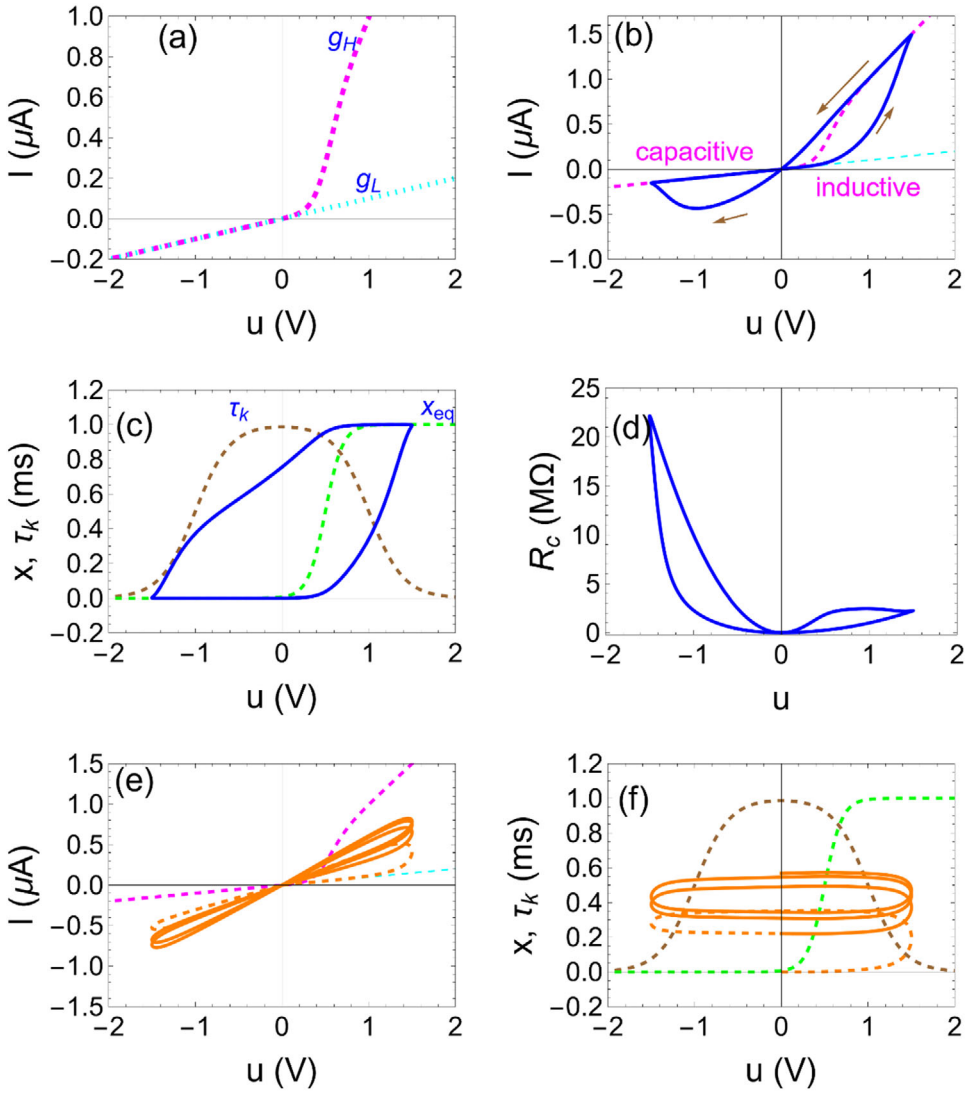

Figure 8. Hysteresis in the CALM model. a) Current voltage curve (purple) indicating the low conductance branch (cyan). b,c,e,f) Hysteresis in $I-V$ curves and memory variable x under sinusoidal stimulation $u = U_0 \sin(\Omega_s t)$ at amplitude $U_0 = 1.5$ V and different frequencies: Blue line $f_\Omega = 0.2$ Hz, b,c) orange line $f_\Omega = 4$ Hz e,f). b,e) Current–voltage loops. The dashed line is the first cycle, and the straight lines are the dc (purple) and low (cyan) conductance. c,f) x-variable loops, indicating the x_{eq} (green) and relaxation time (brown). Initial condition $V_0 = 0$, $x_0 = 0$ (blue), $x_0 = 0.6$ (orange). d) The cord resistance evolution for $f_\Omega = 0.2$ Hz. Model parameters $g_L = 0.1$ μS, $g_H = 1$ μS, $V_m = 0.1$ V, $\tau_0 = 1$ ms, $\tau_M = 1$ ms, $V_{Bx} = 0.5$ V, $V_A = 1$ V, $n_A = 2$, $V_{B\tau} = -1$ V, and $n_D = 2$.

variables—τ_m, τ_h, and τ_n—are a mathematical reflection of the physical speed at which channel gates respond to voltage. They establish the characteristic timescales over which ion channel gates respond to changes in membrane voltage and they explain how a neuron times and regulates the phases of an action potential.

These relaxation times are strongly voltage-dependent and exhibit a distinct nonlinear, inverted U-shaped profile, with a maximum (slowest response) near a particular voltage, as shown in **Figure 10**, and exponentially decreasing at voltages further away from this point. Mechanistically, this means that channel gates respond most slowly around specific voltages—typically near the threshold for action potential initiation—while becoming increasingly fast at hyperpolarized or highly depolarized extremes. This behavior results from the underlying exponential voltage dependence of the opening and closing rate constants α, β, which govern the probability transitions of channel states. The transition rates of each type of channel become apparent if we write the relaxation equation as[49]

$$\frac{dx}{dt} = \alpha_\tau (u)(1-x) - \beta_\tau (u)\, x \tag{18}$$

Comparing Equations (13) and (18), it follows that the relaxation time is

$$\tau_k (u) = \frac{1}{\alpha_\tau + \beta_\tau} \tag{19}$$

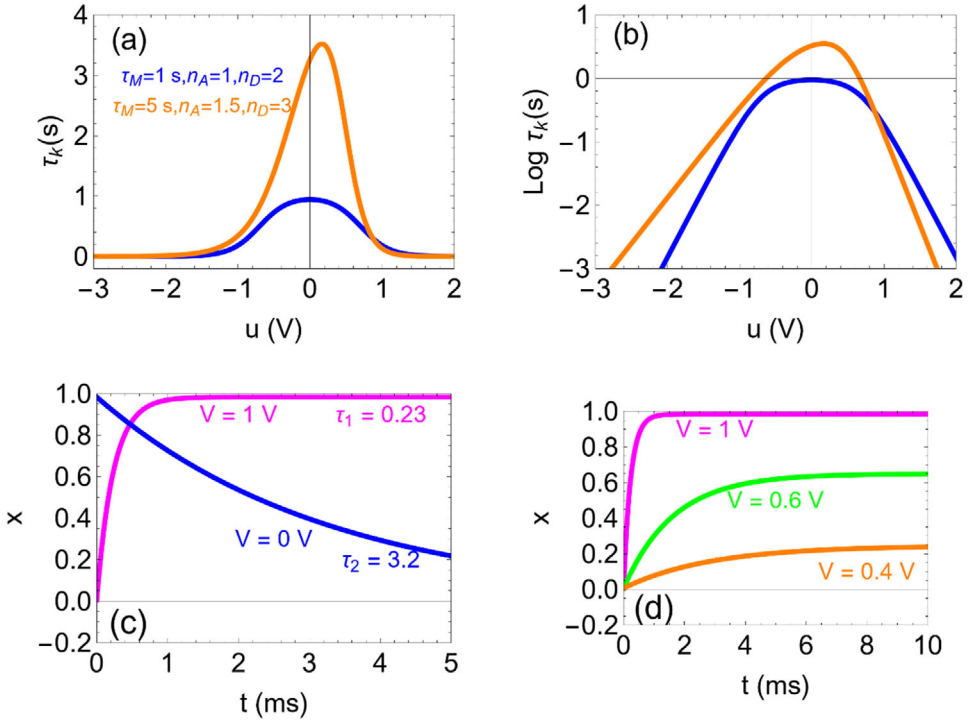

Figure 9. a,b) Relaxation time in the CALM model with different parameters as indicated. c,d) Time transient of x to the target voltage indicated. Model parameters $g_L = 0.1\ \mu S$, $g_H = 1\ \mu S$, $V_m = 0.1\ V$, $\tau_0 = 1\ ms$, $\tau_M = 1\ ms$, $V_{Bx} = 0.5\ V$, $V_A = 0.7\ V$, $n_A = 2$, $V_{B\tau} = 0\ V$, and $n_D = 3$.

with the detailed balance condition

$$\frac{\alpha_\tau}{\beta_\tau} = e^{(u-V_{B\tau})/V_m} \tag{20}$$

The detailed relaxation properties depend on selectivity, conductance, voltage-dependent activation, and fast inactivation of the protein sodium and potassium channels proteins.[95]

In the case of artificial nanopores and nanochannels the cause for rectification arises from the asymmetry in the geometry of the nanopore and/or the distribution of surface charges and their polarities along the sidewalls of the nanopore.[48] The voltage-dependent relaxation time of these systems can be modeled considering the current flow required to change the charge density inside the pore.[96,97] The relaxation time can be considerably enhanced by using gel electrolytes.[98]

The form of the relaxation time can be investigated by voltage steps, as the $\tau_k(u)$ is given by the switching time at each voltage. To view this special property of the CALM models, consider a voltage step from V_0 to V_1, with associated equilibrium values x_0, x_1. Equation (13) can be readily integrated with the result

$$x\ (t) = x_1 + \left(x_0 - x_1\right) e^{-t/\tau_1} \tag{21}$$

There is an exponential time dependence, with the characteristic time $\tau_1 = \tau_k\ (V_1)$ associated to the target voltage. This produces an exponential rise in the case $x_1 > x_0$, and exponential decay when $x_0 > x_1$, as shown in Figure 9c. The current rise time decreases when the final voltage is larger, according to the property of the relaxation time, as illustrated in Figure 9d. These features are well observed in **Figure 11a**.[99] and temperature activation of

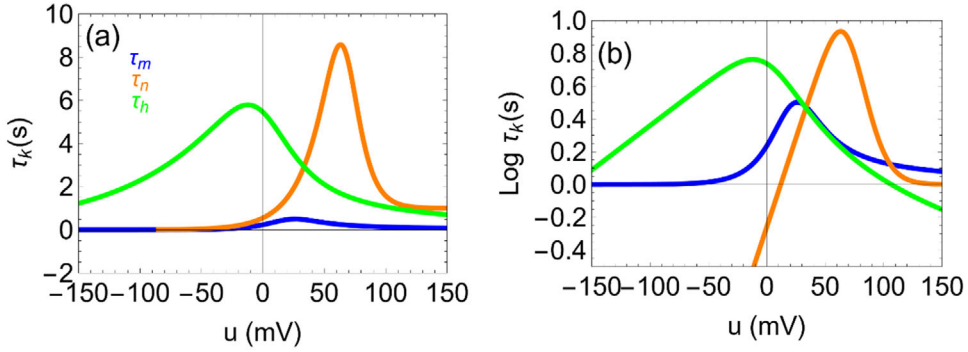

Figure 10. Relaxation times in Hodgkin–Huxley model. a) Linear and b) vertical log scale.

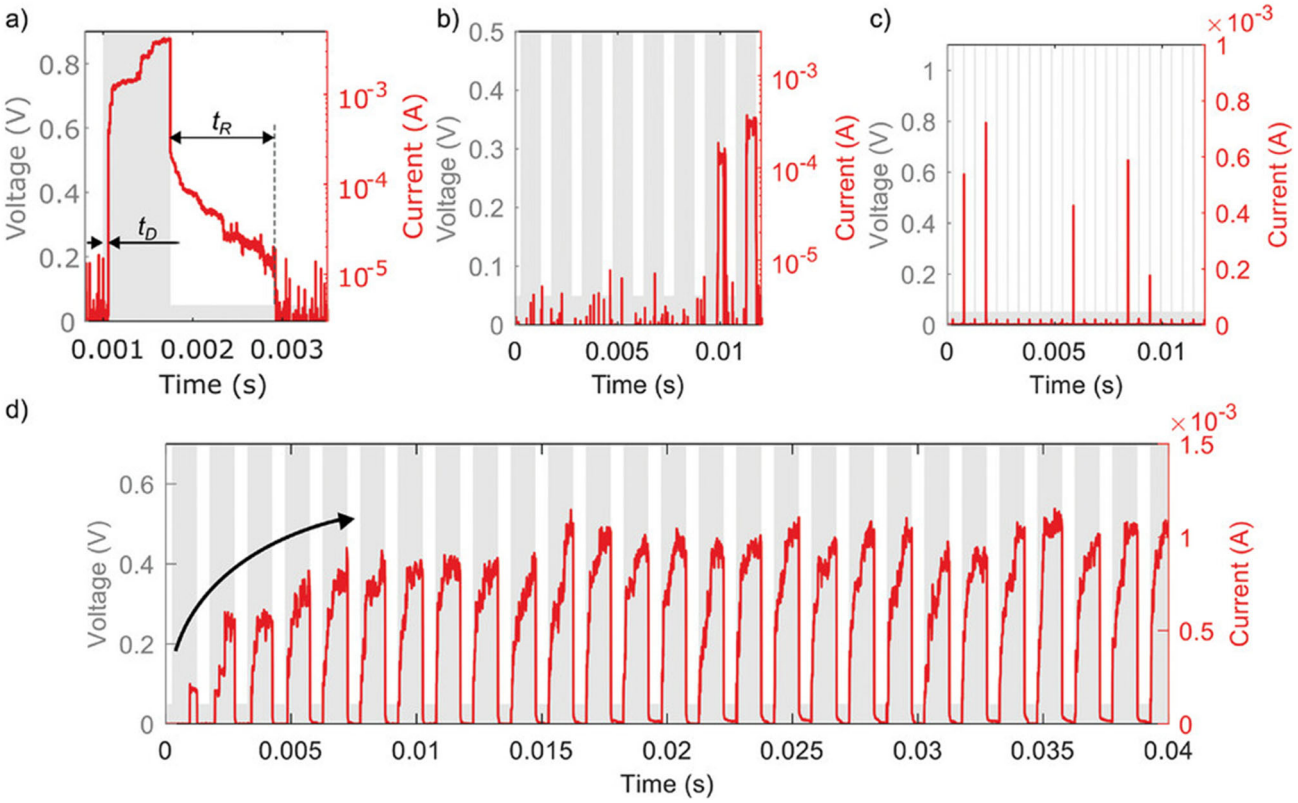

Figure 11. Representative examples of operations on a 50 nm Ag/10 nm SiO_x/30 nm Pt device. In all plots, the left *y* axis is referred to the applied voltage (gray regions), the right *y* axis is referred to the current flowing through the device (red line). a) Response to single voltage pulse, with indication of the delay time, t_D, after which the device switches from HRS to LRS and relaxation time, t_R, defining the time—after withdrawing the pulse voltage—at which the device returns to HRS (pulse width t_p= 0.75 ms, pulse voltage, V_p = 0.9 V). b) Representative indication of wake-up phase in which a few pulses must be accumulated before the switching to occur (t_p = 1 ms, V_p= 0.5 V, interval, t_i= 0.5 ms). c) Representative example of stochastic switching (t_p = 10 µs, V_p = 1.1 V, t_i = 0.5 ms). d) Representative example of cumulative switching: in a first phase the current increases from pulse to pulse (accumulative effect); in a second phase the current eventually stabilizes to a constant average current value (t_p= = 1 ms, V_p= 0.7 V, t_i = 0.5 ms). Reproduced with permission from under the terms of the Creative Commons Attribution (CC BY 4.0) license.[99]

the relaxation time has been presented as well.[100]

The relaxation time is a strong function of the voltage in two-terminal resistance switches and analog memristors based on ionic motion,[2,24,101–103] It is generally observed that the electrochemical processes for filament formation, including nucleation, charge transfer, and mixed charge/ion drift, produces exponential voltage-time relationship.[104] As follows from the previous discussion, the relaxation time is directly related to the switching time, that has been amply investigated in solid state memristors. An overview of the switching dependence on voltage in solid state memristors[94] shows an exponential relationship between the time required to switch the device and the applied pulse amplitude, corresponding to the general property outlined in Figure 9.

5. Hysteresis

The standard analysis of memristors uses the cycling of current–voltage curves at different frequencies (or triangular voltage ramps, as in cyclic voltammetry).[105–107] The resistive switching effect creates large hysteresis loops in the *set* and *reset* processes that are highly informative for the synaptical memory change as we discuss in the following.

5.1. Inductive and Capacitive Cycling Curves

To view hysteresis effects, the voltage u is swept at amplitude U_0, constant angular frequency Ω_s, and frequency $f_\Omega = \Omega_s/2\pi$ as follows

$$u = U_0 \sin\left(\Omega_s t\right) \tag{22}$$

The results are shown in Figure 8b–f. Figure 8b–e shows the *I*–*V* curves at two different frequencies: slow (blue) and fast (orange), respectively, for the system of Figure 8a. In the blue curve, when the voltage starts to increase, the transition from the low to the high conductance line occurs, which is associated with resistive switching. This is an effect of the evolution of the memory conductance variable shown in Figure 8c. In Figure 8b, at first the conductance stays at the low value $x = 0$, but once $V > V_{Bx}$, and when the relaxation time becomes short, it transitions to the value 1, with the associated large conductance g_H.

This $x = 1$ is the value in the first part of the return cycle, so that the current follows the high conductance line. But below the onset voltage $V_{Bx} = 0.5$ V of x_{eq}, the high conductance does not exist, hence the x must decay to zero (again the rapidity is

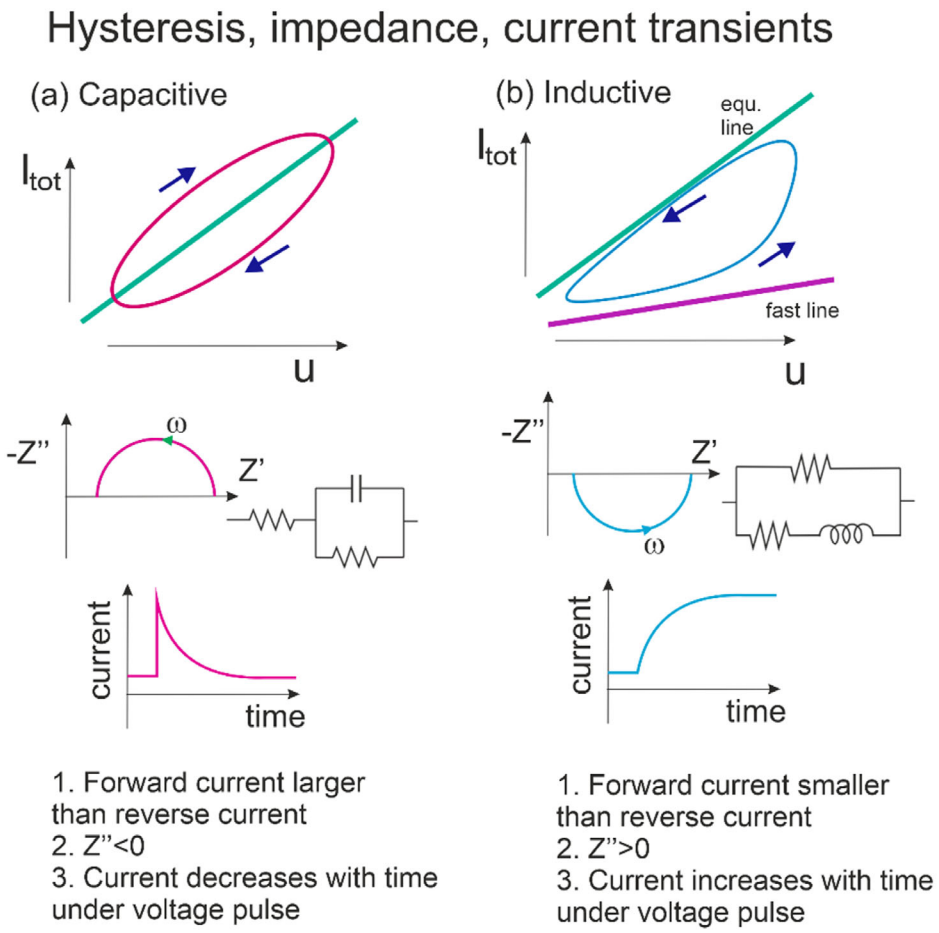

Figure 12. Scheme of the types of hysteresis, and the related impedance and transient current response.

controlled by the relaxation time), and then it stays at the low value $x = 0$. The orange curve in Figure 8e is obtained by cycling the system at a higher frequency. The stationary cycles of positive current lie below the line of high conductance, which cannot be achieved at this cycling rate. This is confirmed by Figure 8f, which shows that the $x < 1$ in this case.

In Figure 8b, the I–V curve makes a self-crossing at the origin. It is counterclockwise at $V > 0$, and clockwise at $V < 0$. These domains have been termed "inductive" ($V > 0$) and "capacitive" ($V < 0$) in a general assessment of hysteresis in memristors and chemical inductors.[108] This denomination is due to the different behaviors of the impedance response, and the transient response, explained in general terms in **Figure 12**. The capacitive (Figure 12a) and inductive (Figure 12b) domains of hysteresis have been amply discussed in specific systems using the frequency-domain method of impedance spectroscopy.[49,109–111] The CALM model of Equations (10–14) leads to the equivalent circuit of Figure 1e,[90] which produces the required synaptic properties.[89] The current transients consist on a rise for the inductive process, and a decay for the capacitive process, as shown in Figure 9c.[45]

One example to confirm the basic inductive-capacitive dichotomy is shown in **Figure 13**.[112] The impedance (well represented by the model as in Figure 1e).[97] measured at positive voltages shows a clear inductor loop at low frequencies, while the impedance measured at negative voltages shows a capacitive response. In both cases, there is a membrane capacitance C_m response at high frequency, and it must be noted that the low-frequency capacitive response at negative voltage arises from the same mechanism that produces the chemical inductor. Therefore, both the inductor and capacitor arise from the conduction current in Equation (12), combined with the relaxation effect in Equation (13). In this sense, the conductance-activated models, such as the CALM model, go beyond the basic properties of the chemical inductor.[46] In fact, the inductor becomes negative and transforms into a positive capacitance.[90]

In more complex systems, the transition from capacitive to inductive hysteresis may occur at a higher voltage, as shown in Figure 2.[50,113] This is in agreement with the potentiation and depression occurring at the two sides of the V_{th} that was mentioned earlier.

5.2. Switching Criteria

Let us summarize the previous results. The temporal evolution of the $I-V$ curve under voltage cycling is represented in Figure 8b. We observe the *set* process at positive voltage, where the current

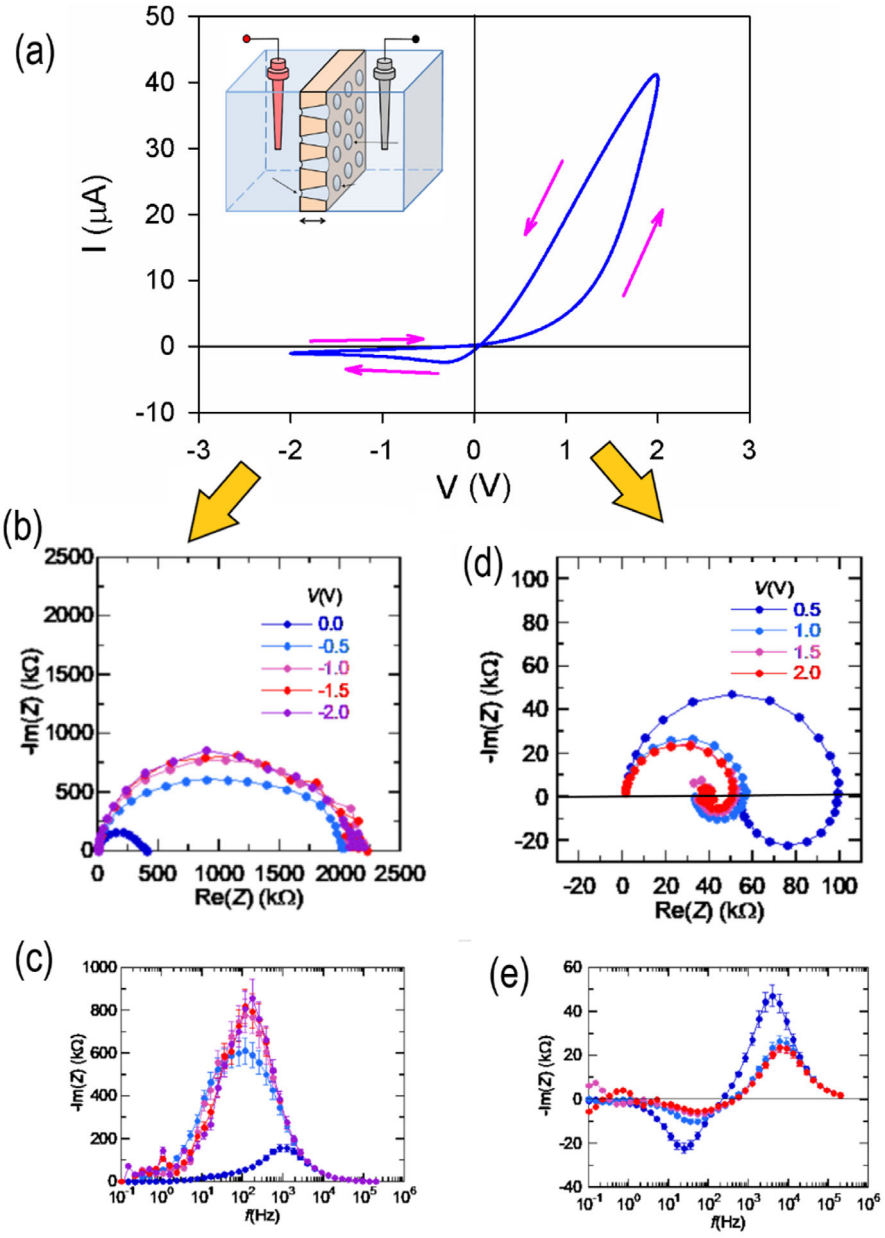

Figure 13. a) Current–voltage curve measured at a frequency of f_Ω = 10 Hz for a multipore membrane in 100 mM KCl solution at neutral pH. The inset shows the electrochemical cell with the membrane. b) The impedance spectra at different reverse voltages, with the corresponding bode plot of the imaginary part of the impedance in (c). d,e) are the impedance spectra and bode plots at forward voltage. Adapted with permission.[112] Copyright 2024, Elsevier.

increases because the conductance passes $g_L \rightarrow g_H$ (inductive domain) and the *reset* process at the negative voltage, when the system returns to the HRS, $g_H \rightarrow g_L$ (capacitive domain).

We would like to emphasize the distinction between the instantaneous "cord" resistance that is defined as[73]

$$R_c = \frac{V}{I_{tot}} \tag{23}$$

and the synaptic conductance σ. Equation (23) is a popular expression in memristor models instead of Equation (1).[114] The cord conductance shown in Figure 8d has useful properties[73] but it is not highly informative to the change of synaptical functionalities. The evolution of the memory variable cannot be directly tracked experimentally in the current (which is also influenced by the voltage), and the progression of x is very different from that of R_c.

The key approach for a better understanding is that the instantaneous synaptic weight σ is determined by the evolution of the variable x. We can summarize the insight to evolution hysteresis curves in the following statements. The temporal changes of x are governed by two main factors

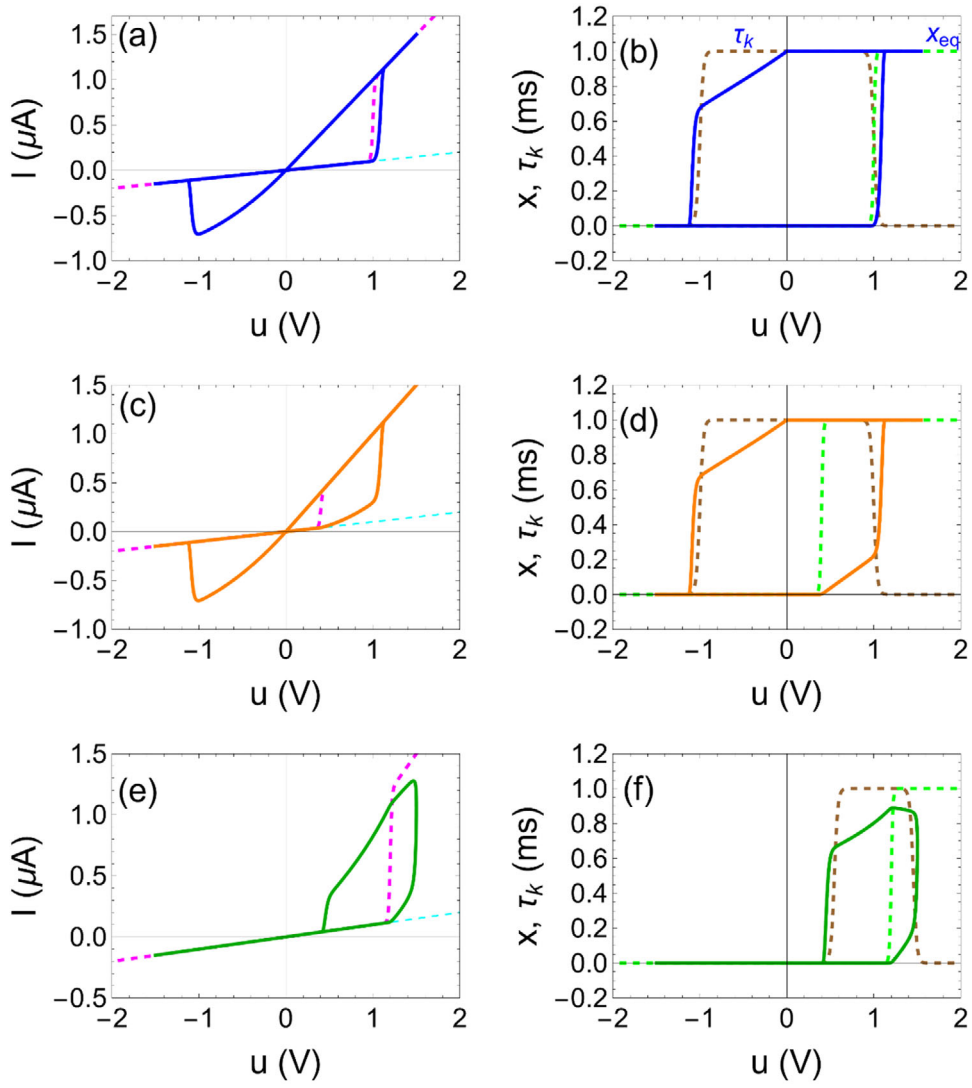

Figure 14. A model with abrupt switching. a,c,e) Hysteresis current–voltage loops under sinusoidal stimulation $u = U_0 \sin(\Omega_s t)$. The dashed line is the first cycle, and the straight lines are the low and high conductance. b,d,f) x-variable loops, indicating the x_{eq} (dotted) relaxation time (dashed), at amplitude $U_0 =$ 1.5 V and cycling frequency $f_\Omega =$ 0.3 Hz, $f_\Omega =$ 3 Hz, Initial condition $V_0 = 0$, $x_0 = 0$. Model parameters $g_L =$ 0.1 μS, $g_H =$ 1 μS, $V_m =$ 0.01 V, $\tau_0 =$ 1 ms, $\tau_M =$ 1 ms, $V_A =$ 1 V, $n_A = 2$, $V_{Br} = 0$ V, $n_D = 2$. Blue line a,b): $V_{Bx} =$ 1 V; orange line c,d) $V_{Bx} =$ 0.4 V. Dark green line e,f): $\tau_0 =$ 0.1 ms, $\tau_M =$ 1 ms, $V_A =$ 1.5 V, $n_A = 2$, $V_{Br} =$ 1 V, $n_D = 2$, $V_{Bx} =$ 1.2 V.

(a) The "Thermodynamic Constraint" determined by quasiequilibrium considerations of the slow curve in Figure 8c: The transition $x = 0 \rightarrow 1$ occurs only when $u > V_{Bx}$. Conversely, the transition $x = 1 \rightarrow 0$ occurs only when $u < V_{Bx}$.

(b) The "Kinetic Constraint" that holds when the system is displaced dynamically by an external stimulus. It is determined by the relaxation time τ_k: The transition $x = 0 \rightarrow 1$ and the transition $x = 1 \rightarrow 0$ occur at a velocity determined by $1/\tau_k$ at the respective voltage.

The criterion A is obvious from the construction of the model. This criterion has the main origin in the modeling of voltage-gate ion channels in Hodgkin–Huxley (HH) model. The criterion B, also introduced originally in HH, causes hysteresis and a set of rich dynamical behaviors.

5.3. Abrupt or Gradual Switching

For the application of memristors as synapses, a multilevel/multistate analog resistive switching is usually required,[22–24,35,55,115–117,118–122] as mentioned before, rather than the abrupt switching that is preferred in digital nonvolatile memory storage applications.[123] By the "Kinetic Constraint" discussed before, the relaxation times, $\tau_k(u)$, dictate whether the current transition in a memristor occurs abruptly, as in digital memristors, or increases gradually, as in an analog-type memristor.[91] Figure 8 represents the typical gradual analog

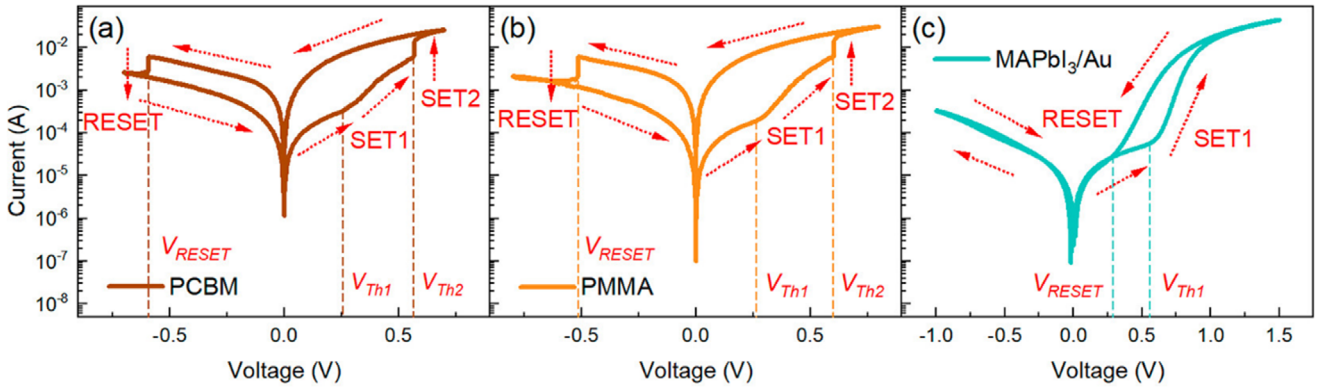

Figure 15. Characteristic *I–V* curves on the semilog scale of halide perovskite ($MAPbI_3$) memristor devices with thin undoped a) PCBM and b) PMMA buffer layers exhibiting nonvolatile bipolar resistive switching, and c) the $MAPbI_3$/Au device exhibiting volatile unipolar resistive switching. The arrows indicate the scan direction and the corresponding SET and RESET processes with their respective threshold voltages. Reproduced with permission.[124] Copyright 2023, American Chemical Society.

response. **Figure** 14a–d shows two cases where the steepness parameter V_m is much smaller than in Figure 8, producing an abrupt rise. In Figure 14a,b, the onset of x and the decay of $\tau_k(u)$ occur at the same voltage, and the current rises suddenly in the inductive cycle when this "threshold" voltage is found. But in Figure 14c,d, it is $V_{Bx} < V_A$ (Equations (14) and (15)) and there is a domain $V_{Bx} < V < V_A$ where the current raises slowly, as the relaxation time is long. When $V \approx V_A$ the relaxation time decays, and occurs the abrupt final switching of the current. This two-step mechanism has been observed experimentally,[124] as shown in **Figure 15** for halide perovskite memristors with different buffer layers.

Figure 14e,f shows an example of volatile memristor using the same CALM model. There is no difference in structure and materials between volatile and nonvolatile memristors, and both volatile and nonvolatile properties could be obtained in one device at different compliance currents.[125] Furthermore both characteristics can be found in the same material by modulating the gradual resistance change through different device structures or specifically programmed external stimuli.[123] In fact, a type of memristor can be transformed from volatile to nonvolatile by modification of the contact[36,126] or chemical treatment.[33] In the case of Figure 15c, this is achieved by changing the buffer layer. The modulations between digital (abrupt switching) and analog (gradual switching) systems, classified by the variation in conductance states, enable the development of versatile multifunctional memristor and synaptic devices. By controlling molecular dynamics through temperature,[127] a wide spectrum of memristor properties—including bipolar, unipolar, nonvolatile, and volatile behaviors—can be achieved within a single device. This spectrum also encompasses sharp transitions as well as gradual analog changes.

Biological neurons generate impulses between 1 and 50 Hz, and sometimes, during pulses, they can burst to several hundred Hz. Volatile memristors, in particular, are directly applicable for replicating neuron dynamics by defining the leakage time constant for membrane voltage. Neurons need to integrate spatiotemporal correlations of patterns across many spatial and temporal scales. Neurons in the first layers close to the sensors typically process small spatial and temporal scales, while neurons in higher, more abstract layers collect extracted features that range over larger spatial and temporal scales.[128] Thus, memristors can be engineered to provide fast volatile time constants in the range of few milliseconds for rapid basic feature extraction (like oriented edges in vision or the sound of consonants in audio) to many-days biometric patterns in biomedical signals.[129]

Additionally, it has been recently demonstrated that memristors with both nonvolatile (long-term plasticity) and volatile (short-term plasticity) properties have enhanced recognition capabilities for dynamically changing input stimuli. The nonvolatile component can trigger a first recognition based on a familiar pattern, while the volatile component aids in maintaining and tracking the recognition while the stimulus is dynamically changing.[130] This generalizes to the metaplasticity concept, with new devices being presented and applied to more challenging computational problems[131,132]

6. Transient Responses and Potentiation

Neuromorphic computation schemes are mainly based on the effects of trains of voltage pulses (including the concept of a single-pulse train) that mimic the repetitive action potential that occurs when a biological neuron fires. A synapse is situated between two nodes (Figure 1a) and receives voltage stimulation from spike trains from both neurons. In essence, a voltage difference acts on the synapsis element and modifies the x property, which determines the σ weight for the next computation step. The dynamic variation of the x property, influenced by the properties of stimuli, such as frequency, duration, amplitude, and synchronization between pre- and postsynaptic neurons, underpins key biological functions essential for brain-like computation. These include short-term and long-term plasticity, SRDP, PPF, STDP, and others,[11,23,25,55–59] as discussed earlier.

To explain these functions, we use the insights obtained in the previous sections about the cycling and impedance response for the analysis of the main question, which is the synaptical device response to consecutive voltage pulses of the same or of different signs. As shown in Figure 8b,c, we present the results at two simultaneous levels. One is the response of the current in the electrical device. The other is the evolution of the memory variable

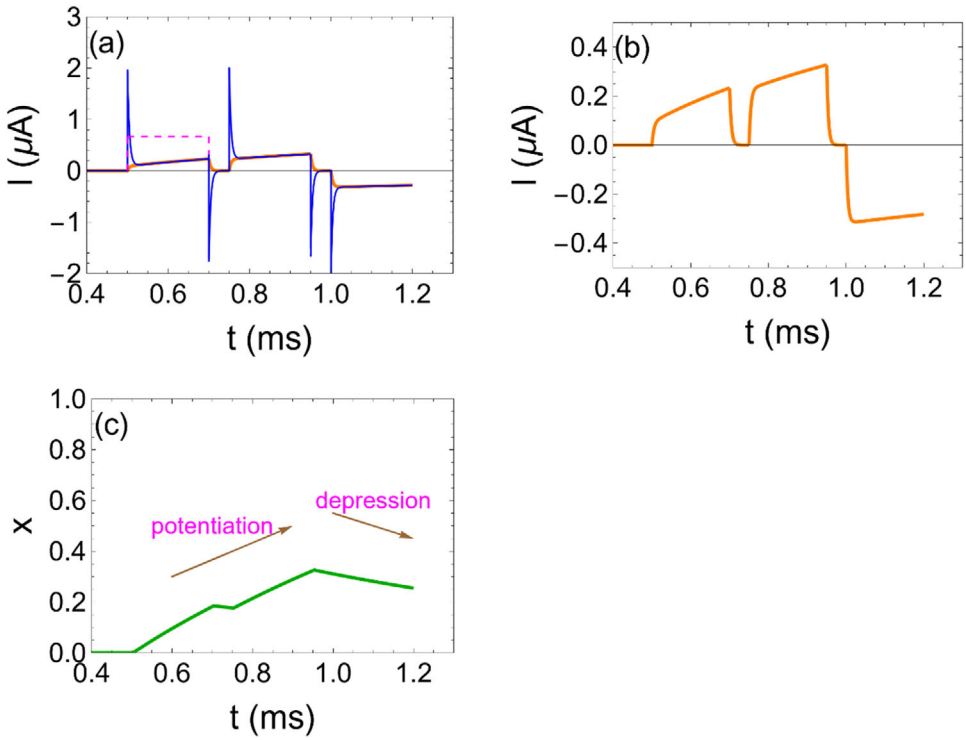

Figure 16. Current response to three voltage pulses applied to the CALM model: (ΔV, ΔV, $-\Delta V$). Transient parameters $V_0 = 0$ V, $\Delta V = 2$ V, $\Delta t_p =$ 0.2 ms, $\Delta t_r = 0.05$ ms initial condition $u_0 = 0$, $x_0 = 0$. a) The blue line is the total current, and the dashed magenta line is the equilibrium current under the applied voltage. Orange line is the conduction current I_{cond} shown in (b). c) Memory variable. Relaxation times: τ_k (V_0) = 1 ms, τ_k ($V_0 + \Delta V$) = 0.016 ms. The dashed line is the final equilibrium value at $V_0 + \Delta V$. Model parameters $g_L = 0.1$ μS, $g_H = 1$ μS, $g_s = 2$ μS, $C_m = 0.01\ 10^{-9}$ F, V_m = 0.1 V, $\tau_0 = 1$ ms, $\tau_M = 1$ ms, $V_{Bx} = 0.5$ V, $n_A = 2$, $V_A = 1$ V, $g_s = 5$ μS, and $C_m = 0.05\ 10^{-9}$ F.

x. As we are using a CALM model in which $\sigma = x$, the state of x immediately tells us the evolution of the synaptic weight that we can use in computation. In other systems, it will always be possible to measure the transient current, but the tracking of σ could require a *read* procedure. Otherwise, if the time evolution of x can be obtained from a suitable dynamical model, the $\sigma(x)$ can be followed for a required application, for example, by the addition of various parallel channels as in HH model.

We investigate the response of the CALM model of Equations (11–15) to a train of voltage pulses (or spikes) that change the voltage from V_0 to $V_0 + \Delta V$. The time dependent applied voltage is

$$V_{app}(t) = V_0 + \Delta V\, \theta(t - t_0)\ \theta(t_0 + \Delta t_p - t) \tag{24}$$

in terms of the unit step function θ. The duration of the polarization pulse is Δt_p, and then the original voltage $V_{app} = V_0$ is applied during inter-spike time Δt_r. Then, the square stimulus is repeated.

The results of applying two positive pulses and one negative pulse are shown in **Figure 16a**.[73,89] The blue line is the total current I_{tot} in Equation (11), and the orange line is the conduction current in Equation (12).

Immediately after the onset of ΔV, the capacitor is charged through the series resistance, which causes a positive spike, i.e., the "fast capacitive current." This spike is inverted when the voltage pulse is disconnected in Figure 16a. The short capacitive spikes are clearly observed in Figures 2 and 3.

Thereafter, the inductive mechanism causes a rise in the current. It involves the transition between fast and slow conduction current to a degree x, so the current increases with time, as discussed in the hysteresis curves. This current rise is associated with the increase of the memory variable, which determines the device conductance. To illustrate the behavior, in Figure 16b, we show only the conduction current, which displays more clearly the increase of the conductance with time during the applied pulse, which can also be observed in Figures 2 and 3. In Figure 16c, we show the evolution of the memory variable $x(t)$. This property controls the effective synaptic weight.

During the resting time between voltage steps in Figure 16, the voltage is turned to $V = 0$, thus the conduction current is forced to decay to 0. Nevertheless, we can observe in Figure 16b that in the second step the current starts from a value slightly lower than the final current in the previous cycle. This is because the evolution of the memory variable is different from that of the current, as shown in the plot in Figure 16c. We can also observe that a negative voltage pulse (following the positive pulses) decreases the x value, in accordance with the hysteresis curves shown in Figure 8, causing depression. In general, depending on the specific synaptic devices' dynamic equations, one can engineer a specific shape of spikes to achieve a desired spike-timing-dependent-plasticity (STDP) learning rule.

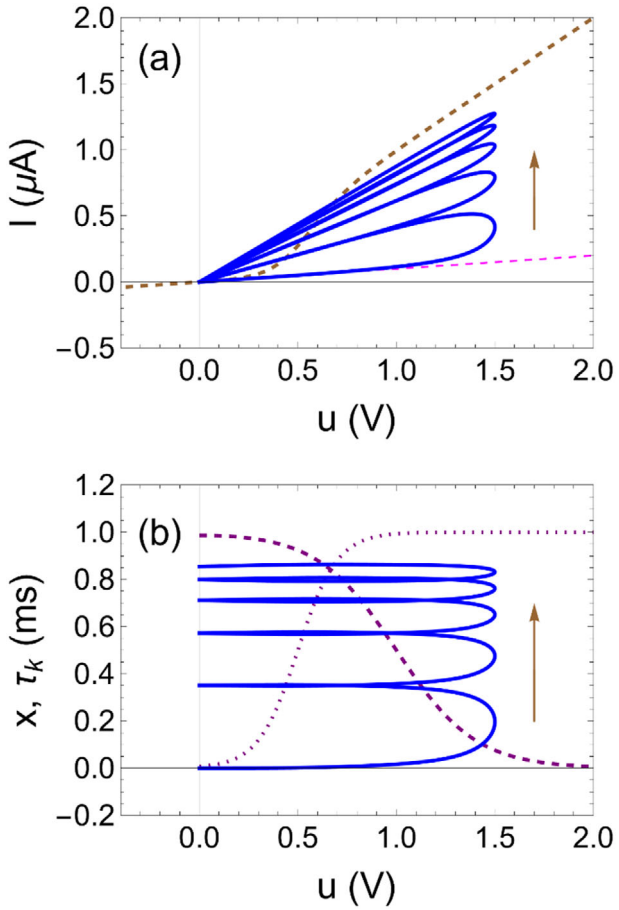

Figure 17. Representation of potentiation in $I-V$ curves. Consecutive sinusoidal stimulation $u = U_0 \sin(\Omega_s t)$ in the positive voltage side. a) Current–voltage loops, the dashed lines are the low and high conductance lines. b) x-variable loops, at amplitude $U_0 = 1.5$ V and cycling frequency $f_\Omega = 5$ Hz, Initial condition $V_0 = 0$, $x_0 = 0$. Model parameters $g_L = 0.1$ μS, $g_H = 1$ μS, $V_m = 0.1$ V, $\tau_0 = 1$ ms, $\tau_M = 1$ ms, $V_{Bx} = 0.5$ V, $V_A = 1$ V, $n_A = 2$, $V_B = -1$ V, $n_D = 2$.

We have already remarked that the progression of x-variable indicating the internal conductance is very different from that of the cord resistance R_c. In the voltage pulses of Figure 16b, we obtain a low current when $V \approx 0$, but the internal conductivity can be high, far from the equilibrium value. This is the reason for using a small *read* voltage, that reveals the storage of conductance. Normally, a *read* operation is performed at a low voltage to detect the current without perturbing the state. However, we remark that the *read* operation in $x_{eq}(V_{read})$ may detect a significant change, depending on the relaxation time and the time at which the value at V_{read} is read. During hardware-in-the-loop training of neural networks, it is recommended to perform this *read* operation, at least after a time of programming equivalent to its relaxation time constant.[133,134]

In the case of positive voltage cycling in **Figure 17a**, the evolution of the current in potentiation can be similarly obtained.[23,25] By repeating the voltage cycling of Figure 8 only in the positive voltage side, we obtain a progressive increase of the x variable, as shown in Figure 17b, since only the inductive stimulus occurs, and the depression part of the cycle is not applied. Then we obtain in Figure 17a the characteristic potentiation $I-V$ curves shown in Figure 4a.

Based on the analysis of the consecutive transients, we can understand many potentiation-depression protocols used in the literature, as in Figures 4 and 5. For example, **Figure 18a–d** shows the conduction current and memory variable under trains of voltage pulses that differ by the interspike time. The characteristic response times correspond to nanochannel synapsis as those of Figure 2.

For the short Δt_r (orange) in Figure 18a, the current raises to the equilibrium value, but for longer Δt_r (green, (c)), this is not possible since there is a loss of x during each resting cycle. This is the well-known frequency dependence of the synapse stimulation,[135] termed SRDP. The spike-rate-dependent characteristic is similar to that of biological synapses and is attributed to the temporal interaction between the excitatory postsynaptic current (EPSC) and the spike.[25] In Figure 18e–h, we apply another type of train in which short pulses are followed by a long resting time. We can find negligible potentiation for long rest time, Figure 18e,f, or significant potentiation if the rest time is shorter than the relaxation time, so that decay of x is not complete when the new pulse arrives, Figure 18g,h. This explains the experimental observations in Figures 4 and 5.

Another significant property is the variation of the response time according to the strength of the stimulation (potentiation).[136] This property is shown in **Figure 19a,b**. By making pulses of different target voltage, the relaxation time that actuates during the polarization time is significantly different. In the green signal Figure 19a,b, we obtain that the stimulation at high voltage is completed by the corresponding inductor mechanism at 1 ms, while the orange signal at low voltage takes a longer time.

The next question we consider is the depression of the synapse. From the point of view of the memory variable, a large value of x is removed by applying pulses in the opposite voltage direction.[45] This is observed in the hysteresis curves of Figure 8. If we start from the point at $V = 0$ with x being low, voltage pulses in the capacitive region can do nothing, since the x cannot be further lowered. This is shown in the orange line of Figure 19c,d. However, if we start from a large value of x, as in the green line, the depression process occurs, and the x is lowered according to the relaxation time.

Based on these properties, we can interpret typical potentiation/depression curves in the literature with reference to the hysteresis curves. In Figure 2e,[40] we observed that the positive pulses produce potentiation, and then the train of negative pulses produces depression. However, in Figure 2f, the positive pulses occur in the capacitive region, in consequence there is no activation of conductance, and the resulting current does not change, hence there is no potentiation or depression. But when negative pulses are applied in Figure 2f, they occur in the inductive region, and they cause potentiation.

In **Figure 20b**, the effect of pulses of different duration is compared, by observing the evolution of current as function of the number of pulses. The short polarization pulse (red) provides the gradual rise of the current due to the chemical inductor effect. However, for the longer pulse (blue) the activation of the inductor is completed within one pulse, and the pulses provide a

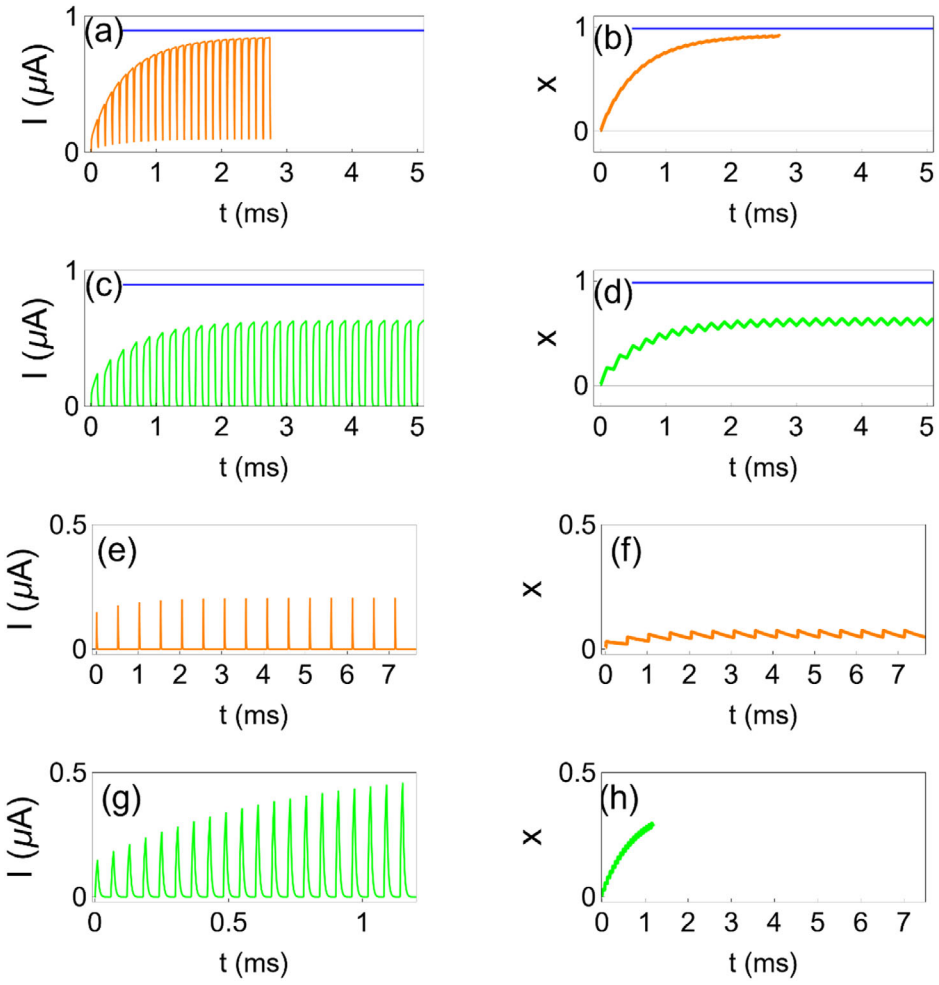

Figure 18. Current (left) and memory (right) variable in response to a train of 50 voltage pulses. a–d) Transient parameters $V_0 = 0\ V$, $\Delta V = 1\ V$, $\Delta t_p = 0.1$ ms, and the two cases: $\Delta t_r = 0.1$ ms (green), a,b) $\Delta t_r = 0.01$ ms (orange). c,d) The blue line is the final equilibrium value of the current at $V_0 + \Delta V$. Model parameters $g_L = 0.1\ \mu S$, $g_H = 1\ \mu S$, $V_m = 0.1\ V$, $\tau_0 = 1$ ms, $\tau_M = 1$ ms, $V_{Bx} = 0.5\ V$, $n_A = 2$, $V_A = 1\ V$, $g_s = 5\ \mu S$, $C_m = 0.05\ 10^{-9}$ F. Initial condition $V_0 = 0$, $x_0 = 0$. Relaxation times: $\tau_k\ (V_0) = 1$ ms, $\tau_k\ (V_0 + \Delta V) = 0.016$ ms. e–h) Transient parameters $V_0 = 0\ V$, $\Delta V = 1.5\ V$, $\Delta t_p = 0.01$ ms, and the two cases: $\Delta t_r = 0.5$ ms e,f orange), $\Delta t_r = 0.05$ ms g,h green). Model parameters $g_L = 0.1\ \mu S$, $g_H = 1\ \mu S$, $V_m = 0.1\ V$, $\tau_0 = 1$ ms, $\tau_M = 1$ ms, $V_{Bx} = 0.5\ V$, $n_A = 2$, $V_A = 1\ V$, $g_s = 5\ \mu S$, $C_m = 0.05\ 10^{-9}$ F. Initial condition $u_0 = 0$, $x_0 = 0$. Relaxation times: $\tau_k\ (V_0) = 1$ ms, $\tau_k\ (V_0 + \Delta V) = 0.016$ ms.

constant current. In the depression voltage side, the removal of the current is completed in the first pulse, and thereafter there is no further response. Figure 20d shows the resultant PPF response of the same system.

Learning-forgetting-relearning behaviors can be implemented by controlling these voltage pulses with varied time intervals.[137,138] Learning-relearning process can be obtained by applying the subsequent pulses before the complete decay of the pre-pulses, where the relearning process is faster than learning with a smaller number of pulses. On the other hand, the Ebbinghaus forgetting nature can be shown in the case of less rehearsed or less exposed information, which is caused by the fast decay. So, the different time scales and pulses control is important to mimic real human brain cognition system.

Dynamic properties of synapses can indeed be very helpful at system level to make computations more efficient. For example, recently there has been a trend in training not only synaptic weights in multilayer neural networks, but also train a delay for each synapse.[139,140] This results in smaller networks with the same computational performance. Hardware implementations of synapses with dynamic properties have been shown to be successful for the realization of self-learning large-size attractor networks comprising up to 256 neurons with 128k dynamic synapses.[141] Complex dynamical synapses hardware realizations have also been demonstrated for building soft winner-takes-all decision networks.[142] Smaller networks of four neurons with synapses capable of reproducing the response properties of five different types of chemical synapses, including both excitatory (AMPA, NMDA) and inhibitory ($GABA_A$, $GABA_C$, glycine) ionotropic, have been demonstrated to provide greater flexibility for the design and implementation of biologically realistic neural networks with energy-efficient population codes on neuromorphic chips.[142]

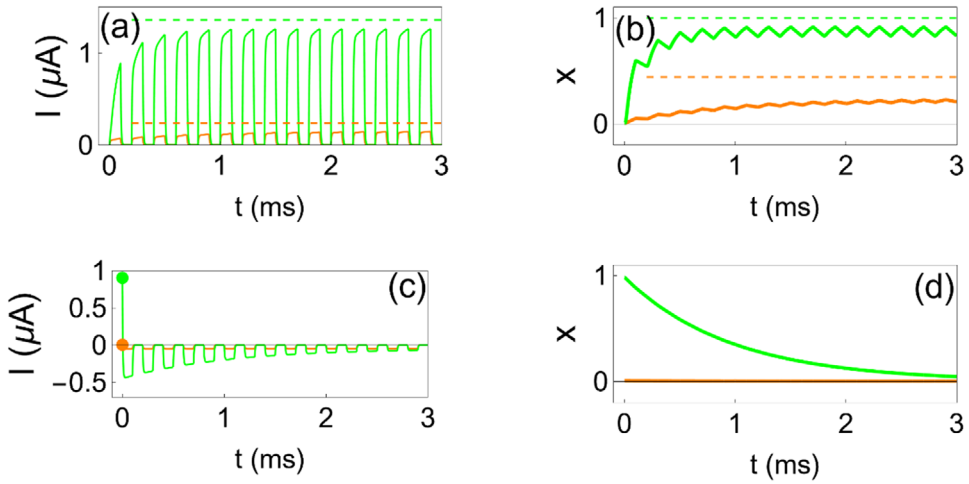

Figure 19. Current and memory variable variations over time factor in the a,b) potentiation/c,d) depression progress. a) Current and b) memory variable in response to a train of 30 pulses. Transient parameters $V_0 = 0\ V$, $\Delta t_p = \Delta t_r = 0.1$ ms, and the two cases: $\Delta V = 1.5\ V$ (green), $\Delta V = 0.5\ V$ (orange). The dashed line is the final equilibrium value at $V_0 + \Delta V$. Model parameters $g_L = 0.1\ \mu S$, $g_H = 1\ \mu S$, $V_m = 0.1$ V, $\tau_0 = 1$ ms, $\tau_M = 1$ ms, $V_{Bx} = 0.5$ V, $n_A = 2$, $V_A = 1$ V, $g_s = 5\ \mu S$, $C_m = 0.05\ 10^{-9}$ F . Initial condition $u_0 = 0$, $x_0 = 0$. Relaxation times: τ_k (1.5 V) = 0.92 ms, τ_k (0.5 V) = 0.076 ms. c) Current and d) memory variable in response to a train of 30 voltage pulses. Transient parameters $V_0 = 0\ V$, $\Delta V = -0.5\ V$, $\Delta t_p = \Delta t_r = 0.1$ ms, and the two cases of initial condition $u_0 = 0$, $x_0 = 0$ (orange) and $u_0 = 0.91$, $x_0 = 0.98$ (green), indicated by dots. $\Delta V = 1.5\ V$ (green), (orange). Model parameters $g_L = 0.1\ \mu S$, $g_H = 1\ \mu S$, $V_m = 0.1$ V, $\tau_0 = 1$ ms, $\tau_M = 1$ ms, $V_{Bx} = 0.5$ V, $n_A = 2$, $V_A = 1$ V, $g_s = 5\ \mu S$, $C_m = 0.05\ 10^{-9}$ F .

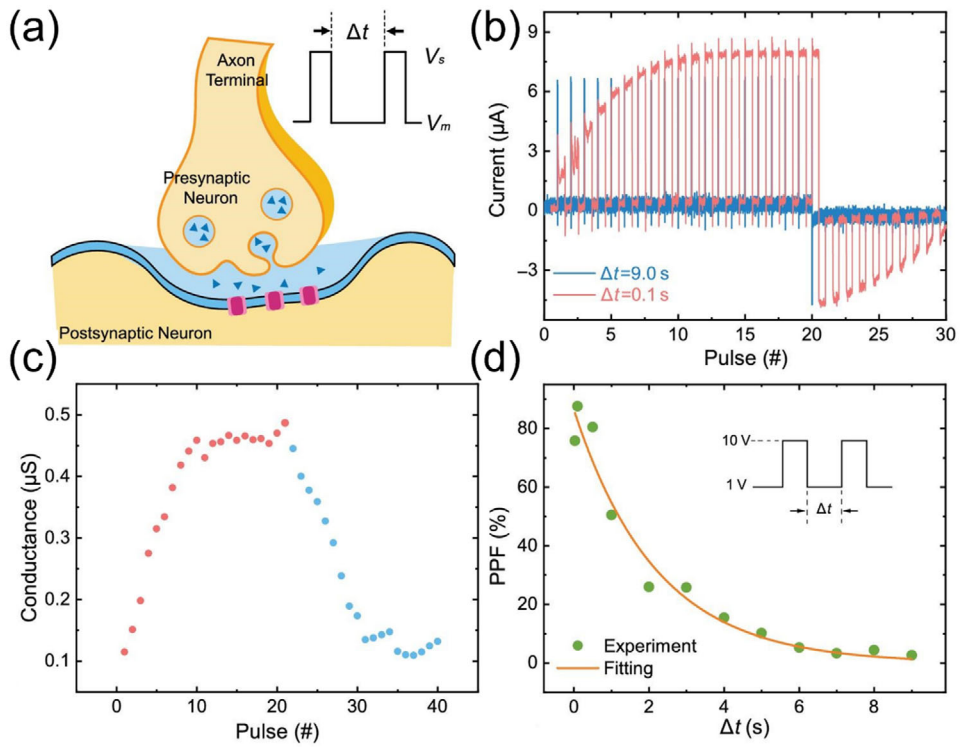

Figure 20. a) Schematic picture of a biological synapse with spikes with a resting time Δt. b) The measured current of a single polymer nanopore under periodic spikes for the SRDP process in adaptive Hebbian learning. c) The conductance switches under positive and negative spikes. d) Paired-pulse facilitation decreases as the time interval between voltage spikes increases and matches well with an exponential fitting. Reproduced from licensed under a Creative Commons Attribution (CC BY 4.0) license.[40]

7. Model Limitations and Extensions

The CALM model (Equations (11–13)) applies to very broad classes of memristors, and the utility is demonstrated recently in a variety of synaptic materials and devices.[49,89–92] It is justified if the concentration of ionic defects forming a filament is proportional to the conductivity.[25]

The model is, however, not general, as there may be other types of memory variables, with nonlinear x-adaptation functions.[70,143,144] We have mentioned that HH model contains the quasilinear properties of the CALM model in the x-variables relaxation Equations (7–9). However, in HH model the state variable is not the conductivity, in fact as observed in Equation (6) the model is described by 3 state variables that determine the conductances of two currents in parallel, for the sodium and potassium channels, and furthermore the conductances are not x-linear, as observed in Equation (6). In fact Hodgkin and Huxley[80] found very different forms of short and long time behavior of transient curves: a simple exponential decay in repolarization, but a delayed increase in depolarization. They thus proposed that the potassium conductance is proportional to a *power* of a variable that obeys a first-order equation. Thus the quasilinear relaxation property persists, and each variable relaxes independently, so that each obeys Equation (21). The transient ionic currents of biological neurons have been amply investigated to elucidate these properties.[82,145]

In a classification scheme,[146] memristors and neuron elements are attributed an order that corresponds to the number of differential equations required to describe them. However, we have seen that other properties such as the linearity of the relaxation equations have a great influence on the complexity of the response. One example is the synaptical model of Equations (11) and (13). It contains two differential equations, for the variables (u, x), however the capacitive term in Equation (11) is a spectator for the synapsis response, as we remarked in Figure 16, hence only one differential equation describes well the synaptical function, which is comprised by the model (12, 13). On the other hand, neuron oscillators can be also described by Equations (11) and (13), provided that one of the variables contains a negative resistance. In oscillator memristors, however, the two differential equations are essential, since they are the minimal number required for a Hopf bifurcation.[87,88]

Besides augmenting the number of states variables, another cause of dynamical complexity is their interdependence. When two states variables are interlinked it is possible to obtain a Hopf bifurcation by a dynamical negative resistance.[147] Another example is obtained by using two coupled state variables that produce synapse adaptation.[148] The presence of coupled state variables in memristor models enables the emulation of biological phenomena such as metaplasticity, activity-dependent thresholds, and triplet- or quadruplet-based learning rules.[100,149] These are key aspects of the Bienenstock–Cooper–Munro (BCM) learning rule,[64,65] described before, in which low-frequency stimulus leads to depression, while high-frequency stimulus leads to potentiation. One solution to obtain these effects is to complement the dynamical relaxation equation for x with additional equations that indicate variable thresholds adapting to both LTP and LTD), which reproduces the refractory time in the weight modification.[150]

8. Different Physical Stimulations

The input–output signals applied to the bio-inspired memristors to induce the learning and memorizing/forgetting processes are reported not only for the electrical signals but also for other physical stimuli. In particular, the optical stimuli, such as the light of a specific wavelength band, which stimulates the device during the stimuli that cause the change of conductance, is an example in **Figure 21**. The input–output physical stimulation to induce the potentiation and depression processes combining light and electrical signals can be classified into four typical categories depending on which process the electrical and optical stimuli are given: 1) input (electrical signal)–output (electrical signal), 2) input (electrical signal)–output (optical signal), 3) input (optical signal)–output (electrical signal), and 4) input (optical signal)–output (optical signal).[153]

To implement artificial synapses, the first category that stimulates both input and output signals with electrical signals is the most reported form and can be seen in many of the examples we have previously described here (Figures 2–5). Synaptic devices powered by electrical stimulus show relatively easy drive controls, but face issues such as switching speed. To solve these issues, the external optical signal was presented to the device alone or in conjunction with the external electrical stimulation.

The second or third category using optical stimulation for either input or output signals has recently been attempted in various ways in memristors using photoactive materials such as perovskites,[154] semiconductor materials,[155] 2D materials,[156] QD materials,[157] etc. This is because optical stimulations provide complementary points, such as low power consumption, low crosstalk in the integrated systems, various bandwidths, and fast response speed with light irradiation intensity, time, and light pulse control.[158] The combination of electrical and optical stimulation of synapses can be used for schemes of associative learning and latent inhibition.[159]

One step further from this, devices that lead all the input/output sources for the learning-memorizing/forgetting process to optical stimulation are developing despite their limitations in bidirectional positive-negative spikes and large-scale which are challenging to control because they have advantages, such as signal transmission speed, similar mimicking system with a human brain, and unnecessary circuit reduction.[152,153,155] For this, the last category, all-optical synapses, has also been reported in such a way as using specific material with the flexibility of the wavelength band required for input/output or using an interference system that can use an optional wavelength band.[160] For achieving all-optical input–output neuromorphic systems, various materials with optical reactive properties, such as photoluminescence,[152] photochromism,[161] photorefraction,[162] etc., are reported.

In addition to the electrical stimulation for the conductance change that we explained in the preceding sections, the basic principles that operate synaptical systems do not deviate much from the basic principles that cause potentiation and depression in other physical stimuli, such as optical stimulations. For example in Figure 21b, the trapped carrier density in a perovskite crystal is the x − property, and it can be observed that the memory property persists when the photoluminescence has vanished,[152,163] as the response to a further

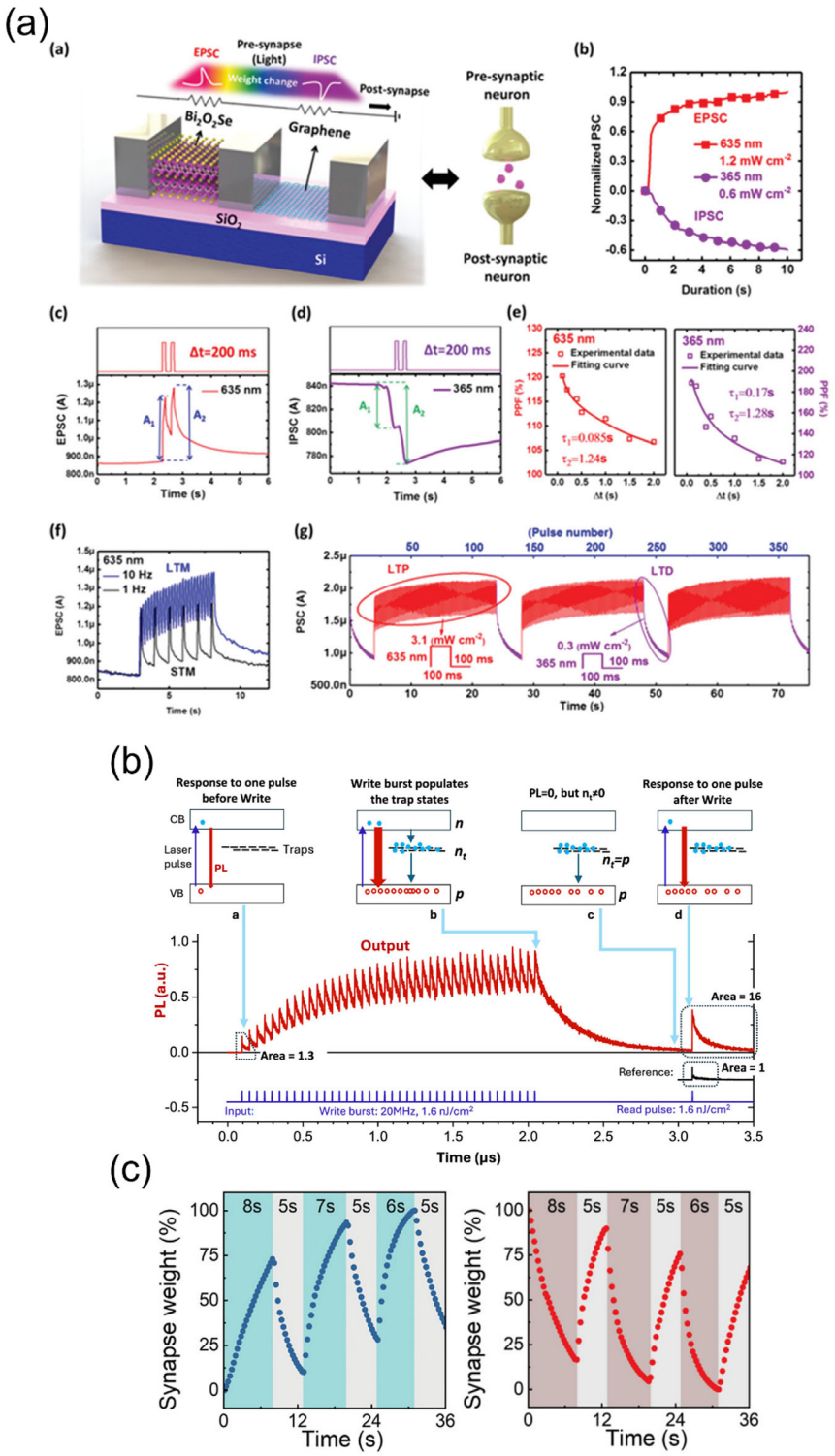

Figure 21. Synaptic functions in various optically synaptic devices. a) Bi_2O_2Se/graphene optoelectronic synapse with optical stimuli administered at wavelengths of 635 and 365 nm to emulate excitatory and inhibitory behaviors, respectively. Biological synaptic characteristics, such as EPSC, IPSC, LTP, and LTD according to illumination duration time, time interval, frequency, etc. Reproduced with permission.[151] Copyright 2020, John Wiley and Sons. b) General mechanism and demonstration of the short-term memory in the $CsPbBr_3$ thin film memlumor (memory + luminophore). Time correlated single photon counting (TCSPC) photoluminescence (PL) response (red) to a Write burst consisted of 40 pulses separated by 50 ns (pulse fluence 1.6 nJ cm^{-2}) followed by one reading pulse after 1 μs delay (laser pulses shown by blue). Reproduced with permission.[152] Copyright 2024, American Chemical Society. c) Excitatory (blue) and inhibitory (red) synaptic behaviors with control light of 405 nm and signal light of 1310 nm in $CsPbBr_3$ single crystal-based artificial synapse device. Reproduced with permission.[153] Copyright 2024, John Wiley and Sons.

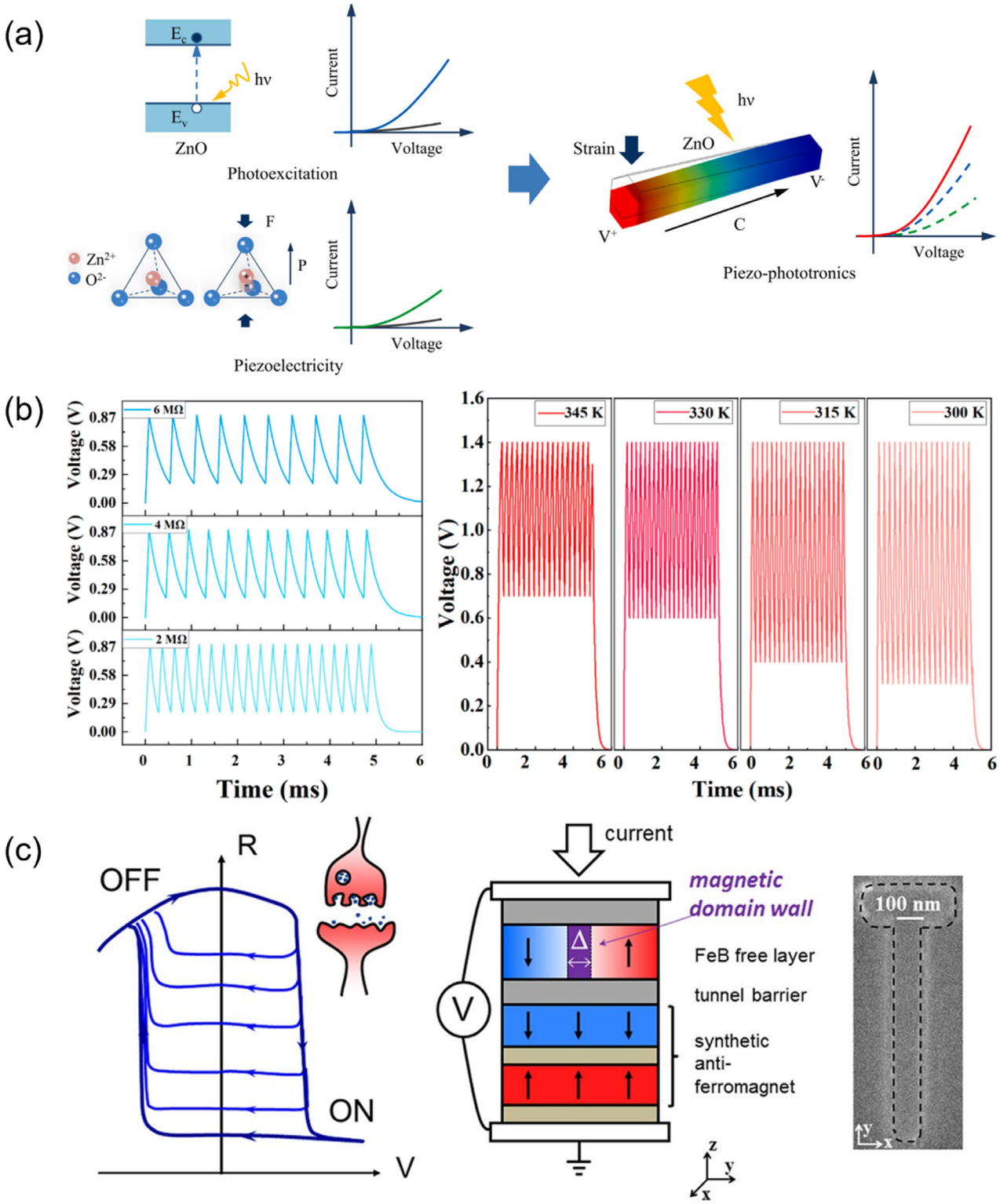

Figure 22. Various physical stimulated synaptic devices. a) ZnO micro/nanowire-based photonic synapse using the piezo-phototronic effect. Reproduced with permission from Reproduced from licensed under a Creative Commons Attribution (CC BY 4.0) license.[164] Copyright the authors. b) Impulse simulation response of neuronal circuits of Bi_2SE_3-based memristor simulated with oscillation characteristics of the thermoreceptor in response to various values of resistance and threshold voltage in neuron circuit. Reproduced with permission from licensed under a Creative Commons Attribution (CC BY 4.0) license.[165] Copyright. c) Schematic synaptic memristor with MgO based magnetic tunnel junction with the domain wall in the FeB free layer. Reproduced with permission from licensed under a Creative Commons Attribution (CC BY 4.0) license. Copyright the authors.[166]

pulse when $x > 0$ is much higher than the initial response when $x \approx 0$.

The systems through these optical stimulations have a rather complex response, such as light interference, scattering, reflection, etc., but basically induce synaptic weight changes by going through processes, such as overlapping and reflection, depending on the intensity of the optical source, the irradiation time, and the time interval, as shown in Figure 21.

Recently, optical synapses have also been implemented in integrated systems using photonic optical circuits, where conductance changes are realized through photoexcited trap occupation or light-induced phase transitions in chalcogenide or perovskite materials. In particular, integrated optical memristors built with waveguide-coupled phase-change materials enable local synaptic processing and ultrafast, high-bandwidth communication through refractive index modulation.[164,167] These devices have demonstrated high-density integration and low crosstalk, suitable for large-scale optical neuromorphic networks.

Beyond optical inputs, other physical stimuli—including mechanical pressure, temperature, humidity, and magnetic fields, etc.,—have also been shown to modulate the synaptic behavior in memristive devices in **Figure 22**. Pressure-sensitive memristors, typically based on piezoelectric or flexible oxide layers, exhibit conductance change due to strain-induced lattice deformation or bandgap modulation (Figure 22a).[164,168] Similarly, thermal stimuli can enhance ionic mobility, accelerating conductive filament formation or vacancies redistribution in oxide-based devices (Figure 22b).[165] Magnetic field-responsive synapses, often utilizing magneto-resistive or spintronic structures, enable modulation of resistance states via spin-polarized current or domain wall motion (Figure 22c).[166,169]

These physical effects provide distinct internal mechanisms, such as light-induced properties, phase transitions, ionic drift, piezoelectric strain, or spin transport, that that can be leveraged to mimic diverse synaptic dynamics. Integrating such multimodal stimuli into artificial synaptic architectures enhances computational richness and allows for biologically inspired functions like sensory fusion and adaptive control. Thus, integrating different physical inputs into synaptic device operations not only improves synaptic functionality but also accesses new computational mechanisms such as environmental response learning and adaptive sensory-motor coupling. From a physical proposal point of view, our synapse review here shows the possibility that it can be extended to various physical stimulations as well.

9. Discussion

We have shown that the synaptic response can be described by the combination of two factors: 1) a conduction process that depends on an internal state variable, 2) the $x-$ variable is affected by rectification at an onset voltage and memory (delay of response with respect to stimulus) effects. These properties impart an intrinsic chemical inductor mechanism that is responsible for the potentiation phenomenon. The velocity of potentiation, i.e., the time change of x, is determined by the system's relaxation time, which can change orders of magnitude, modifying the response to voltage and frequency.[97] The "analog" memristor that shows gradual potentiation according to the hysteresis curves in Figure 8, and the "abrupt" resistive switching memristor of Figure 14, are both characterized by the same CALM model, but in the latter case the τ_k changes suddenly at a threshold voltage, while in the former a diversity of hysteresis curves can be observed.[91]

Our discussion provides a broad view of synaptic phenomena for systems that are controlled by a single internal variable that governs the system's conductance. The basic potentiation/depression cycles can be interpreted based on the hysteresis response of current–voltage curves. Furthermore, the $x-$ linearity property, provides a direct interpretation of the device switching times in terms of the internal relaxation time function.

One can use more advanced models and microscopic simulations involving physical equations adapted to the specific situation. However, such general models must include the central traits that we have explained, and it is useful to address the specific components of the physical models, particularly concerning relaxation time properties. Obtaining a physical interpretation of the memory variable x, related to filamentary formation, ionic valence change, interface barrier lowering, etc., is an important complementary study. The general effects we have described can arise not only from ionic redistribution, but also from electronic trapping[111] and in light-induced systems.

This model may be extended in several directions to describe different realistic situations. One can consider the combination of memristors in series, parallel, etc. that produces more complex responses,[170] including the complementary memristor obtained by antiserial connection[171] that shows capacitive cycles at both polarities, and the operation of logic gates.[10,41,43] Another important extension is developing models that couple several memory variables that display more complex dynamics to encompass the situations where the basic parameters evolve with time, as in the BCM learning rule.

10. Conclusion

The essential characteristics that lead to the dynamical features producing the learning and forgetting features of artificial synapse devices have been described. It is based on a conductance system in which the high conductance is activated by a memory variable that lags the applied stimulus. Therefore, the hysteresis curves at different cycling rates reveal the essential properties of potentiation and depression in the system.

When it comes to implement physical neuromorphic chips capable of both nonvolatile as well as volatile capabilities, the main challenge is to control independently the parameters for both capabilities. With new memristors being reported in the recent literature featuring both capabilities, it will be necessary to have a good understanding of parameter interdependencies to better engineer the corresponding artificial synapses. In this sense, a unified model as presented here can help in better simulating scaled-up systems and analyzing the impact of low-level parameters on system-level performance.

Acknowledgements

This work was funded by the European Research Council (ERC) via Advanced Grant No. 101097688 (PeroSpiker).

Conflict of Interest

The authors declare no conflict of interest.

Data Availability Statement

The data presented here can be accessed at https://doi.org/10.5281/zenodo.13950252 (Zenodo) under the license CC-BY-4.0 (Creative Commons Attribution-ShareAlike 4.0 International).

Keywords

memristors, neuromorphic computing, synapses

Received: March 6, 2025
Revised: April 18, 2025
Published online: June 17, 2025

[1] D. V. Christensen, R. Dittmann, B. Linares-Barranco, A. Sebastian, L. Gallo, *Neuromorph. Comput. Eng.* **2022**, *2*, 022501.
[2] J. J. Yang, D. B. Strukov, D. R. Stewart, *Nat. Nanotechnol.* **2013**, *8*, 13.
[3] Y. Zhang, Z. Wang, J. Zhu, Y. Yang, M. Rao, W. Song, Y. Zhuo, X. Zhang, M. Cui, L. Shen, R. Huang, J. Joshua Yang, *Appl. Phys. Rev.* **2020**, *7*, 011308.
[4] J. Zhu, T. Zhang, Y. Yang, R. Huang, *Appl. Phys. Rev.* **2020**, *7*, 011312.
[5] H.-K. He, H.-M. Huang, R. Yang, *Neuromorphic Devices for Brain-Inspired Computing*, Wiley-VCH, Germany **2022**, pp. 1–46.
[6] L. I. Zhang, H. W. Tao, C. E. Holt, W. A. Harris, M.-m. Poo, *Nature* **1998**, *395*, 37.
[7] L. O. Chua, K. Sung Mo, *Proc. IEEE* **1976**, *64*, 209.
[8] Y. V. Pershin, M. Di Ventra, *Adv. Phys.* **2011**, *60*, 145.
[9] M.-K. Song, J.-H. Kang, X. Zhang, W. Ji, A. Ascoli, I. Messaris, A. S. Demirkol, B. Dong, S. Aggarwal, W. Wan, S.-M. Hong, S. G. Cardwell, I. Boybat, J.-S. Seo, J.-S. Lee, M. Lanza, H. Yeon, M. Onen, J. Li, B. Yildiz, J. A. del Alamo, S. Kim, S. Choi, G. Milano, C. Ricciardi, L. Alff, Y. Chai, Z. Wang, H. Bhaskaran, M. C. Hersam, et al., *ACS Nano* **2023**, *17*, 11994.
[10] I. Vourkas, G. C. Sirakoulis, *IEEE Circ. Syst. Mag.* **2016**, *16*, 15.
[11] T. Serrano-Gotarredona, T. Masquelier, T. Prodromakis, G. Indiveri, B. Linares-Barranco, *Front. Neurosci.* **2013**, *7*, 2.
[12] K. Yang, J. Joshua Yang, R. Huang, Y. Yang, *Small Sci.* **2022**, *2*, 2100049.
[13] M. Huang, M. Schwacke, M. Onen, J. del Alamo, J. Li, B. Yildiz, *Adv. Mater.* **2023**, *35*, 2205169.
[14] V. K. Sangwan, H.-S. Lee, H. Bergeron, I. Balla, M. E. Beck, K.-S. Chen, M. C. Hersam, *Nature* **2018**, *554*, 500.
[15] R. D. Nikam, M. Kwak, J. Lee, K. G. Rajput, W. Banerjee, H. Hwang, *Sci. Rep.* **2019**, *9*, 18883.
[16] J. Bae, J. Won, T. Kim, S. Choi, H. Kim, S.-H. V. Oh, G. Lee, E. Lee, S. Jeon, M. Kim, H. W. Do, D. Seo, S. Kim, Y. Cho, H. Kang, B. Kim, H. Choi, J. Han, T. Kim, N. Nemati, C. Park, K. Lee, H. Moon, J. Kim, H. Lee, D. W. Davies, D. Kim, S. Kang, B.-K. Yu, J. Kim, et al., *Nat. Mater.* **2024**, *23*, 1402.
[17] S. Y. Kim, J. M. Yang, E. S. Choi, N. G. Park, *Adv. Funct. Mater.* **2020**, *30*, 1.
[18] T. K. Su, W. K. Cheng, C. Y. Chen, W. C. Wang, Y. T. Chuang, G. H. Tan, H. C. Lin, C. H. Hou, C. M. Liu, Y. C. Chang, J.-J. Shyue, K.-C. Wu, H.-W. Lin, *ACS Nano* **2022**, *16*, 12979.
[19] S. Y. Kim, D. A. Park, N. G. Park, *ACS Appl. Electron. Mater.* **2022**, *4*, 2388.
[20] G. Pedretti, D. Ielmini, *Electronics* **2021**, *10*, 1063.
[21] P. Mannocci, M. Farronato, N. Lepri, L. Cattaneo, A. Glukhov, Z. Sun, D. Ielmini, *APL Mach. Learn.* **2023**, *1*, 010902.
[22] J. Q. Yang, R. Wang, Z. P. Wang, Q. Y. Ma, J. Y. Mao, Y. Ren, X. Yang, Y. Zhou, S. T. Han, *Nano Energy* **2020**, *74*, 104828.
[23] S. H. Jo, T. Chang, I. Ebong, B. B. Bhadviya, P. Mazumder, W. Lu, *Nano Lett.* **2010**, *10*, 1297.
[24] N. Ilyas, D. Li, C. Li, X. Jiang, Y. Jiang, W. Li, *Nanoscale Res. Lett.* **2020**, *15*, 30.
[25] Z. Q. Wang, H. Y. Xu, X. H. Li, H. Yu, Y. C. Liu, X. J. Zhu, *Adv. Funct. Mater.* **2012**, *22*, 2759.
[26] J. Chen, Y. Lu, Z. Yang, Y. Li, X. Miao, *Neuromorphic Devices for Brain-Inspired Computing*, Wiley Press, Oxford **2022**, pp. 125–147.
[27] Y. Kim, Y. J. Kwon, D. E. Kwon, K. J. Yoon, J. H. Yoon, S. Yoo, H. J. Kim, T. H. Park, J.-W. Han, K. M. Kim, C. S. Hwang, *Adv. Mater.* **2018**, *30*, 1704320.
[28] T. Ahmed, S. Walia, E. L. H. Mayes, R. Ramanathan, V. Bansal, M. Bhaskaran, S. Sriram, O. Kavehei, *Sci. Rep.* **2019**, *9*, 15404.
[29] R. Yang, K. Terabe, Y. Yao, T. Tsuruoka, T. Hasegawa, J. K. Gimzewski, M. Aono, *Nanotechnology* **2013**, *24*, 384003.
[30] M. Dutta, S. Brivio, S. Spiga, *Adv. Electron. Mater.* **2024**, *10*, 2400221.
[31] D. Kuzum, R. G. D. Jeyasingh, B. Lee, H. S. P. Wong, *Nano Lett.* **2012**, *12*, 2179.
[32] S.-Y. Kim, J.-M. Yang, E.-S. Choi, N.-G. L. Park, *Adv. Funct. Mater.* **2020**, *30*, 2002653.
[33] R. A. John, Y. Demirag, Y. Shynkarenko, Y. Berezovska, N. Ohannessian, M. Payvand, P. Zeng, M. I. Bodnarchuk, F. Krumeich, G. Kara, I. Shorubalko, M. V. Nair, G. A. Cooke, T. Lippert, G. Indiveri, M. V. Kovalenko, *Nat. Commun.* **2022**, *13*, 2074.
[34] L. Zhou, S. Han, H. Liu, Z. He, J. Huang, Y. Mu, Y. Xie, X. Pi, X. Lu, S. Zhou, Y. Hou, *Cell Rep. Phys. Sci.* **2024**, *5*, 102078.
[35] W. Xu, H. Cho, Y.-H. Kim, Y.-T. Kim, C. Wolf, C.-G. Park, T.-W. Lee, *Adv. Mater.* **2016**, *28*, 5916.
[36] N.-K. Pendyala, C. Gonzales, A. Guerrero, *Small Struct.* **2024**, *6*, 2400380.
[37] P. Ramirez, V. Gomez, J. Cervera, S. Mafe, J. Bisquert, *J. Phys. Chem. Lett.* **2023**, *14*, 10930.
[38] D. Shi, W. Wang, Y. Liang, L. Duan, G. Du, Y. Xie, *Nano Lett.* **2023**, *23*, 11662.
[39] T. M. Kamsma, J. Kim, K. Kim, W. Q. Boon, C. Spitoni, J. Park, R. van Roij, *Proc. Natl. Acad. Sci. USA* **2024**, *121*, 2320242121.
[40] X. Zhou, Y. Zong, Y. Wang, M. Sun, D. Shi, W. Wang, G. Du, Y. Xie, *Natl. Sci. Rev.* **2024**, *11*, nwad216.
[41] B. Sabbagh, N. E. Fraiman, A. Fish, G. Yossifon, *ACS Appl. Mat. Int.* **2023**, *15*, 23361.
[42] J. S. Najem, G. J. Taylor, R. J. Weiss, M. S. Hasan, G. Rose, C. D. Schuman, A. Belianinov, C. P. Collier, S. A. Sarles, *ACS Nano* **2018**, *12*, 4702.
[43] T. Emmerich, Y. Teng, N. Ronceray, E. Lopriore, R. Chiesa, A. Chernev, V. Artemov, M. Di Ventra, A. Kis, A. Radenovic, *Nat. Electron.* **2024**, *7*, 271.
[44] E. Covi, S. Brivio, A. Serb, T. Prodromakis, M. Fanciulli, S. Spiga, *Front. Neurosci.* **2016**, *10*, 482.
[45] S.-Y. Kim, H. Zhang, G. Rivera-Sierra, R. Fenollosa, J. Rubio-Magnieto, J. Bisquert, *J. Appl. Phys.* **2025**, *137*, 111101.
[46] J. Bisquert, A. C. I. Guerrero, *J. Am. Chem. Soc.* **2022**, *144*, 5996.
[47] Q. Sheng, Y. Xie, J. Li, X. Wang, J. Xue, *Chem. Commun.* **2017**, *53*, 6125.
[48] Z. S. Siwy, *Adv. Funct. Mater.* **2006**, *16*, 735.
[49] J. H. Bisquert, *Adv. Phys. Res.* **2024**, *3*, 2400029.
[50] C. Gonzales, A. Bou, A. Guerrero, J. Bisquert, *J. Phys. Chem. Lett.* **2024**, *15*, 6496.
[51] F. Alibart, L. Gao, B. D. Hoskins, D. B. Strukov, *Nanotechnology* **2012**, *23*, 3.

[52] M. Patel, D. D. Kumbhar, J. Gosai, M. R. Sekhar, A. T. Mallajosyula, A. Solanki, *Adv. Electron. Mater.* **2023**, *9*, 2200908.
[53] T. Ohno, T. Hasegawa, T. Tsuruoka, K. Terabe, J. K. Gimzewski, M. Aono, *Nat. Mater.* **2011**, *10*, 591.
[54] S. L. Jackman, W. G. Regehr, *Neuron* **2017**, *94*, 447.
[55] M. Prezioso, M. R. Mahmoodi, F. M. Bayat, H. Nili, H. Kim, A. Vincent, D. B. Strukov, *Nat. Commun.* **2018**, *9*, 5311.
[56] M. Prezioso, F. Merrikh Bayat, B. Hoskins, K. Likharev, D. Strukov, *Sci. Rep.* **2016**, *6*, 21331.
[57] S. Song, K. D. Miller, L. F. Abbott, *Nat. Neurosci.* **2000**, *3*, 919.
[58] A. Bofill-i-Petit, A. F. Murray, *IEEE Trans. Neural Networks* **2004**, *15*, 1296.
[59] K. Seo, I. Kim, S. Jung, M. Jo, S. Park, J. Park, J. Shin, K. P. Biju, J. Kong, K. Lee, B. Lee, H. Hwang, *Nanotechnology* **2011**, *22*, 254023.
[60] C. Zamarreño-Ramos, T. Serrano-Gotarredona, L. Camuñas-Mesa, J. Perez-Carrasco, T. Masquelier, B. Linares-Barranco, *Front. Neurosci.* **2011**, *5*, 26.
[61] K. Zarudnyi, A. Mehonic, L. Montesi, M. Buckwell, S. Hudziak, A. J. Kenyon, *Front. Neurosci.* **2018**, *12*, 57.
[62] M. Hellenbrand, B. Bakhit, H. Dou, M. Xiao, M. O. Hill, Z. Sun, A. Mehonic, A. Chen, Q. Jia, H. Wang, J. L. MacManus-Driscoll, *Sci. Adv.* **2023**, *9*, adg1946.
[63] F. Alibart, S. Pleutin, O. Bichler, C. Gamrat, T. Serrano-Gotarredona, B. Linares-Barranco, D. Vuillaume, *Adv. Funct. Mater.* **2012**, *22*, 609.
[64] E. L. Bienenstock, L. N. Cooper, P. W. Munro, *J. Neurosci.* **1982**, *2*, 32.
[65] J. Xiong, R. Yang, J. Shaibo, H.-M. Huang, H.-K. He, W. Zhou, X. B. Guo, *Adv. Funct. Mater.* **2019**, *29*, 1807316.
[66] A. Kirkwood, M. C. Rioult, M. F. Bear, *Nature* **1996**, *381*, 526.
[67] R. Waser, M. Aono, *Nat. Mater.* **2007**, *6*, 833.
[68] M. D. Ventra, Y. V. Pershin, L. O. Chua, *Proc. IEEE* **2009**, *97*, 1717.
[69] T. Prodromakis, C. Toumazou, L. Chua, *Nat. Mater.* **2012**, *11*, 478.
[70] L. Gao, Q. Ren, J. Sun, S.-T. Han, Y. Zhou, *J. Mat. Chem. C* **2021**, *9*, 16859.
[71] Z. Xie, D. Zhang, L. Cheng, C. Li, J. Elia, J. Wu, J. Tian, L. Chen, M. A. Loi, A. Osvet, C. J. Brabec, *ACS Energy Lett.* **2024**, *9*, 948.
[72] S. Liu, J. Guan, L. Yin, L. Zhou, J. Huang, Y. Mu, S. Han, X. Pi, G. Liu, P. Gao, S. Zhou, *J. Phys. Chem. Lett.* **2022**, *13*, 10994.
[73] J. Bisquert, A. Bou, A. Guerrero, E. Hernández-Balaguera, *APL Mach. Learn.* **2023**, *1*, 036101.
[74] E. Hernández-Balaguera, J. Bisquert, *ACS Energy Lett.* **2022**, *7*, 2602.
[75] E. Hernandez-Balaguera, J. Bisquert, *Adv. Funct. Mater.* **2024**, *34*, 2308678.
[76] E. Hernández-Balaguera, L. Munoz-Diaz, A. Bou, B. Romero, B. Ilyassov, A. Guerrero, J. Bisquert, *Neuromorph. Comput. Eng.* **2023**, *3*, 024005.
[77] T. Chang, S.-H. Jo, K.-H. Kim, P. Sheridan, S. Gaba, W. Lu, *Appl. Phys. A* **2011**, *102*, 857.
[78] D. P. Pattnaik, Y. Ushakov, Z. Zhou, P. Borisov, M. D. Cropper, U. W. Wijayantha, A. G. Balanov, S. E. Savel′ev, *Phys. Rev. Appl.* **2023**, *19*, 024065.
[79] L. Chen, C. Li, T. Huang, Y. Chen, S. Wen, J. Qi, *Phys. Lett. A* **2013**, *377*, 3260.
[80] A. L. Hodgkin, A. F. Huxley, *J. Physiol.* **1952**, *117*, 500.
[81] M. Häusser, *Nat. Neurosci.* **2000**, *3*, 1165.
[82] H. R. Wilson, *Spikes, Decisions, and Actions: The Dynamical Foundations of Neuroscience*, Oxford University Press, Walton Street, Oxford **1999**.
[83] A. J. Hopper, H. Beswick-Jones, A. M. Brown, *Adv. Physiol. Educ.* **2022**, *46*, 580.
[84] B. Hille, *Ion Channels of Excitable Membranes*, Sinauer Associates, Sunderland, MA **1992**.
[85] H. Hibino, A. Inanobe, K. Furutani, S. Murakami, I. Findlay, Y. Kurachi, *Physiol. Rev.* **2010**, *90*, 291.
[86] S. Hagiwara, S. Miyazaki, N. P. Rosenthal, *J. Gen. Physiol.* **1976**, *67*, 621.
[87] A. Cordero, J. R. Torregrosa, J. Bisquert, *Phys. Rev. Res.* **2025**, *7*, 013282.
[88] J. Bisquert, R. Fenollosa, A. Cordero, J. R. Torregrosa, *J. Phys. Chem. Lett.* **2025**, *16*, 3616.
[89] J. Bisquert, M. Sánchez-Mateu, A. Bou, C. S. Law, A. Santos, *ChemPhysChem* **2024**, *25*, 202400265.
[90] J. Bisquert, E. Miranda, J. B. Roldan, *PhysChemChemPhys* **2024**, *26*, 13804.
[91] A. Bou, C. Gonzales, P. P. Boix, Y. Vaynzof, A. Guerrero, J. Bisquert, *J. Phys. Chem. Lett.* **2024**, *16*, 69.
[92] E. Miranda, J. Suñé, *IEEE Trans. Nanotechnol.* **2020**, *19*, 837.
[93] E. M. Izhikevich, *Dynamical Systems in Neuroscience*, MIT Press, Cambridge, MA **2007**.
[94] W. Chen, S. Tappertzhofen, H. J. Barnaby, M. N. Kozicki, *J. Electroceram.* **2017**, *39*, 109.
[95] W. A. Catterall, *J. Physiol.* **2012**, *590*, 2577.
[96] J. Cervera, S. Portillo, P. Ramirez, S. Mafe, *Phys. Fluids* **2024**, *36*, 047129.
[97] G. Rivera-Sierra, P. Ramirez, J. Bisquert, A. Bou, *Am. Chem. Soc.* **2025**, *147*, 17529.
[98] Z. Zhang, B. Sabbagh, Y. Chen, G. Yossifon, *ACS Nano* **2024**, *18*, 15025.
[99] M. Dutta, S. Brivio, S. Spiga, *Adv. Electron. Mater.* **2024**, *10*, 2400221.
[100] Z. Wang, S. Joshi, S. E. Savel'ev, H. Jiang, R. Midya, P. Lin, M. Hu, N. Ge, J. P. Strachan, Z. Li, Q. Wu, M. Barnell, G.-L. Li, H. L. Xin, R. S. Williams, Q. Xia, J. J. Yang, *Nat. Mater.* **2017**, *16*, 101.
[101] J. S. Lee, S. Lee, T. W. Noh, *Appl. Phys. Rev.* **2015**, *2*, 031303.
[102] F. Cüppers, S. Menzel, C. Bengel, A. Hardtdegen, M. von Witzleben, U. Böttger, R. Waser, S. Hoffmann-Eifert, *APL Mater.* **2019**, *7*, 091105.
[103] I. Fernandez-Guillen, C. A. Aranda, P. F. Betancur, M. Vallés-Pelarda, C. Momblona, T. S. Ripolles, R. Abargues, P. P. Boix, *Adv. Electron. Mater.* **2024**, *10*, 2300475.
[104] S. Menzel, S. Tappertzhofen, R. Waser, I. Valov, *Phys. Chem. Chem. Phys.* **2013**, *15*, 6945.
[105] L. Chua, *Appl. Phys. A* **2011**, *102*, 765.
[106] M. Lanza, H.-S. P. Wong, E. Pop, D. Ielmini, D. Strukov, B. C. Regan, L. Larcher, M. A. Villena, J. J. Yang, L. Goux, A. Belmonte, Y. Yang, F. M. Puglisi, J. Kang, B. Magyari-Köpe, E. Yalon, A. Kenyon, M. Buckwell, A. Mehonic, A. Shluger, H. Li, T.-H. Hou, B. Hudec, D. Akinwande, R. Ge, S. Ambrogio, J. B. Roldan, E. Miranda, J. Suñe, K. L. Pey, et al., *Adv. Electron. Mater.* **2019**, *5*, 1800143.
[107] J. B. Roldán, E. Miranda, D. Maldonado, A. N. Mikhaylov, N. V. Agudov, A. A. Dubkov, M. N. Koryazhkina, M. B. González, M. A. Villena, S. Poblador, M. Saludes-Tapia, R. Picos, F. Jiménez-Molinos, S. G. Stavrinides, E. Salvador, F. J. Alonso, F. Campabadal, B. Spagnolo, M. Lanza, L. O. Chua, *Adv. Intell. Syst.* **2023**, *5*, 2200338.
[108] J. Bisquert, *PRX Energy* **2023**, *3*, 011001.
[109] J. H. Bisquert, *Adv. Energy Mater.* **2024**, *14*, 2400442.
[110] V. Lopez-Richard, R. S. Wengenroth Silva, O. Lipan, F. Hartmann, *J. Appl. Phys.* **2023**, *133*, 134901.
[111] V. Lopez-Richard, L. A. Meneghetti, G. L. Nogueira, F. Hartmann, C. F. O. Graeff, *Phys. Rev. B* **2024**, *110*, 115306.
[112] P. Ramirez, J. Cervera, S. Nasir, M. Ali, W. Ensinger, S. Mafe, *J. Colloid Interface Sci.* **2024**, *655*, 876.
[113] E. H. Balaguera, J. Bisquert, *ACS Energy Lett.* **2024**, *9*, 478.
[114] L. O. Chua, *Proc. IEEE* **2012**, *100*, 1920.
[115] B. Linares-Barranco, T. Serrano-Gotarredona, *Nat. Precedings* **2009**.
[116] R. Kozma, R. E. Pino, G. E. Pazienza, *Advances in Neuromorphic Memristor Science and Applications*, Springer, New York **2012**.

[117] C. Wang, Z. Si, X. Jiang, A. Malik, Y. Pan, S. Stathopoulos, A. Serb, S. Wang, T. Prodromakis, C. Papavassiliou, *IEEE J. Emerg. Sel. Top. Circuits Syst.* **2022**, *12*, 723.
[118] X. Yang, Z. Xiong, Y. Chen, Y. Ren, L. Zhou, H. Li, Y. Zhou, F. Pan, S.-T. Han, *Nano Energy* **2020**, *78*, 105246.
[119] J. Gong, H. Wei, Y. Ni, S. Zhang, Y. Du, W. Xu, *Mater. Today Phys.* **2021**, *21*, 100540.
[120] S. Ham, S. Choi, H. Cho, S.-I. Na, G. Wang, *Adv. Funct. Mater.* **2019**, *29*, 1806646.
[121] J. Lao, W. Xu, C. Jiang, N. Zhong, B. Tian, H. Lin, C. Luo, J. Travas-sejdic, H. Peng, C.-G. Duan, *J. Mater. Chem. C* **2021**, *9*, 5706.
[122] J. Ding, W. Gao, L. Gao, K. Lu, Y. Liu, J.-L. Sun, Q. Yan, *J. Phys. Chem. Lett.* **2022**, *13*, 7831.
[123] D. Chen, X. Zhi, Y. Xia, S. Li, B. Xi, C. Zhao, X. Wang, *Small* **2023**, *19*, 2301196.
[124] C. Gonzales, A. Guerrero, *J. Phys. Chem. Lett.* **2023**, *14*, 1395.
[125] C. Zhang, J. Shang, W. Xue, H. Tan, L. Pan, X. Yang, S. Guo, J. Hao, G. Liu, R.-W. Li, *Chem. Commun.* **2016**, *52*, 4828.
[126] Z. Shen, C. Zhao, Y. Liu, Y. Qi, I. Z. Mitrovic, L. Yang, C. Zhao, *Solid-State Electron.* **2021**, *186*, 108132.
[127] Many-Body Molecular Interactions in a Memristor. *Adv. Mater.* **2023**, *35*, 2204551.
[128] J. A. Perez-Carrasco, Z. Bo, C. Serrano, B. Acha, T. Serrano-Gotarredona, C. Shouchun, B. Linares-Barranco, *IEEE Trans. Pattern Anal. Mach. Intell.* **2013**, *35*, 2706.
[129] M. Velazquez Lopez, B. Linares-Barranco, J. Lee, H. Erfanijazi, A. Patino-Saucedo, M. Sifalakis, F. Catthoor, K. Myny, *Commun. Eng.* **2024**, *3*, 102.
[130] S. G. Sarwat, B. Kersting, T. Moraitis, V. P. Jonnalagadda, A. Sebastian, *Nat. Nanotechnol.* **2022**, *17*, 507.
[131] C. Weilenmann, A. N. Ziogas, T. Zellweger, K. Portner, M. Mladenović, M. Kaniselvan, T. Moraitis, M. Luisier, A. Emboras, *Nat. Commun.* **2024**, *15*, 6898.
[132] C. Li, X. Zhang, P. Chen, K. Zhou, J. Yu, G. Wu, D. Xiang, H. Jiang, M. Wang, Q. Liu, *iScience* **2023**, *26*, 106315.
[133] H. Erfanijazi, L. A. Camuñas-Mesa, E. Vianello, T. Serrano-Gotarredona, B. Linares-Barranco, *IEEE Trans. Circuits Syst. II* **2024**, *71*, 3685.
[134] E. Esmanhotto, T. Hirtzlin, D. Bonnet, N. Castellani, J.-M. Portal, D. Querlioz, E. Vianello, *Adv. Intell. Syst.* **2022**, *4*, 2200145.
[135] H. Yu, J. Gong, H. Wei, W. Huang, W. Xu, *Mater. Chem. Front.* **2019**, *3*, 941.
[136] F. Zhou, Z. Zhou, J. Chen, T. H. Choy, J. Wang, N. Zhang, Z. Lin, S. Yu, J. Kang, H.-S. P. Wong, Y. Chai, *Nat. Nanotechnol.* **2019**, *14*, 776.
[137] T. S. Rao, S. Kundu, B. Bannur, S. J. George, G. U. Kulkarni, *Nanoscale* **2023**, *15*, 7450.
[138] J. T. Wixted, *Annu. Rev. Psychol.* **2004**, *55*, 235.
[139] A. Patiño-Saucedo, R. Meijer, P. Detteter, A. Yousefzadeh, L. Garrido-Regife, B. Linares-Barranco, M. Sifalakis, in *2024 IEEE International Symposium on Circuits and Systems (ISCAS) 19–22 May 2024*, **2024**, Singapore, pp. 1–5.
[140] I. Hammouamri, I. Khalfaoui-Hassani, T. Masquelier, *arxivPhysics* **2023**, *2306*, 17670.
[141] N. Qiao, H. Mostafa, F. Corradi, M. Osswald, F. Stefanini, D. Sumislawska, G. Indiveri, *Front. Neurosci.* **2015**, *9*, 141.
[142] E. Chicca, F. Stefanini, C. Bartolozzi, G. Indiveri, *Proc. IEEE* **2014**, *10*, 1367.
[143] M. D. Pickett, D. B. Strukov, J. L. Borghetti, J. J. Yang, G. S. Snider, D. R. Stewart, R. S. Williams, *J. Appl. Phys.* **2009**, *106*, 074508.
[144] S. Kvatinsky, E. G. Friedman, A. Kolodny, U. C. Weiser, *IEEE Trans. Circuits Syst. I* **2013**, *60*, 211.
[145] T. F. Weiss, *Cellular Biophysics Electrical Properties*, Vol *2*, MIT, Cambridge **1996**.
[146] S. Kumar, X. Wang, J. P. Strachan, Y. Yang, W. D. Lu, *Nat. Rev. Mater.* **2022**, *7*, 575.
[147] J. Bisquert, A. Guerrero, *J. Phys. Chem. Lett.* **2022**, *13*, 3789.
[148] B. Bao, Y. Zhu, J. Ma, H. Bao, H. Wu, M. Chen, *Sci. China Technol. Sci.* **2021**, *64*, 1107.
[149] R. Yang, H.-M. Huang, X. Guo, *Adv. Electron. Mater.* **2019**, *5*, 1900287.
[150] W. Cai, F. Ellinger, R. Tetzlaff, *IEEE Trans. Biomed. Circuits Syst.* **2015**, *9*, 87.
[151] C.-M. Yang, T.-C. Chen, D. Verma, L.-J. Li, B. Liu, W.-H. Chang, C.-S. Lai, *Adv. Funct. Mater.* **2020**, *30*, 2001598.
[152] A. Marunchenko, J. Kumar, A. Kiligaridis, D. Tatarinov, A. Pushkarev, Y. Vaynzof, I. G. Scheblykin, *ACS Energy Lett.* **2024**, *9*, 2075.
[153] P. Cheng, Z. Liu, J. Zhou, R. Kang, X. Wang, X. Li, X. Zhao, J. Zhao, Z. Zuo, *Adv. Opt. Mater.* **2024**, *12*, 2303306.
[154] N. Yantara, S. E. Ng, D. Sharma, B. Zhou, P.-S. V. Sun, H. M. Chua, N. F. Jamaludin, A. Basu, N. Mathews, *Adv. Mater.* **2024**, *36*, 2305857.
[155] L. Hu, J. Yang, J. Wang, P. Cheng, L. O. Chua, F. Zhuge, *Adv. Funct. Mater.* **2021**, *31*, 2005582.
[156] J. Chen, W. Xu, *eScience* **2023**, *3*, 100178.
[157] Y. Wang, Z. Lv, Q. Liao, H. Shan, J. Chen, Y. Zhou, L. Zhou, X. Chen, V. A. L. Roy, Z. Wang, Z. Xu, Y.-J. Zeng, S.-T. Han, *Adv. Mater.* **2018**, *30*, 1800327.
[158] G. Li, *Light: Sci. Appl.* **2023**, *12*, 24.
[159] S. E. Ng, J. Yang, R. A. John, N. Mathews, *Adv. Funct. Mater.* **2021**, *31*, 2100807.
[160] X. Guo, J. Xiang, Y. Zhang, Y. Su, *Adv. Photonics Res.* **2021**, *2*, 2000212.
[161] X. Zhou, F. Hu, Q. Hou, J. Hu, Y. Wang, X. Chen, *Commun. Mater.* **2024**, *5*, 116.
[162] Q. Wei, H. Dai, H. Shan, H. Li, Z. Cao, X. Chen, *Phys. Rev. B* **2021**, *104*, 235308.
[163] A. Marunchenko, J. Kumar, A. Kiligaridis, S. M. Rao, D. Tatarinov, I. Matchenya, E. Sapozhnikova, R. Ji, O. Telschow, J. Brunner, A. Yulin, A. Pushkarev, Y. Vaynzof, I. G. Scheblykin, *J. Phys. Chem. Lett.* **2024**, *15*, 6256.
[164] C. Lian, C. Vagionas, T. Alexoudi, N. Pleros, N. Youngblood, C. Ríos, *Nanophotonics* **2022**, *11*, 3823.
[165] H. Li, C. Jiang, Q. Hua, *Sensors* **2025**, *25*, 1533.
[166] S. Lequeux, J. Sampaio, V. Cros, K. Yakushiji, A. Fukushima, R. Matsumoto, H. Kubota, S. Yuasa, J. Grollier, *Sci. Rep.* **2016**, *6*, 31510.
[167] N. Youngblood, C. A. Ríos Ocampo, W. H. P. Pernice, H. Bhaskaran, *Nat. Photonics* **2023**, *17*, 561.
[168] G. Hu, H. An, J. Xi, J. Lu, Q. Hua, Z. Peng, *Nano Energy* **2021**, *89*, 106282.
[169] C. H. Marrows, J. Barker, T. A. Moore, T. Moorsom, *npj Spintronics* **2024**, *2*, 12.
[170] P. Ramirez, S. Portillo, J. Cervera, J. Bisquert, S. Mafe, *Phys. Rev. E* **2024**, *109*, 044803.
[171] E. Linn, R. Rosezin, C. Kügeler, R. Waser, *Nat. Mater.* **2010**, *9*, 403.